Atomistic theory of the moiré Hofstadter butterfly in magic-angle graphene

Alina Wania Rodrigues [1,*] Maciej Bieniek [2,3,†] Paweł Potasz [4] Daniel Miravet [1] Ronny Thomale,[2]
Marek Korkusiński [5,1] and Paweł Hawrylak [1]

[1]*Department of Physics, University of Ottawa, Ottawa, Ontario, K1N 6N5, Canada*
[2]*Institut für Theoretische Physik und Astrophysik, Universität Würzburg, 97074 Würzburg, Germany*
[3]*Institute of Theoretical Physics, Wrocław University of Science and Technology, Wybrzeże Wyspiańskiego 27, 50-370 Wrocław, Poland*
[4]*Institute of Physics, Faculty of Physics, Astronomy and Informatics, Nicolaus Copernicus University, Grudziądzka 5, 87-100 Toruń, Poland*
[5]*Emerging Technologies Division, National Research Council of Canada, Ottawa, Ontario K1A 0R6, Canada*

We present here a Hofstadter's butterfly spectrum for the magic-angle twisted bilayer graphene obtained using an *ab initio*-based multimillion-atom tight-binding model. We incorporate a hexagonal boron nitride substrate and out-of-plane atomic relaxation. The effects of a magnetic field are introduced via the Peierls modification of the long-range tight-binding matrix elements and the Zeeman spin splitting effects. A nanoribbon geometry is studied, and the quantum size effects for the sample widths up to 1 μm are analyzed both for a large energy window and for the flat band around the Fermi level. For sufficiently wide ribbons, where the role of the finite geometry is minimized, we obtain and plot the Hofstadter spectrum and identify the in-gap Chern numbers by counting the total number of chiral edge states crossing these gaps. Subsequently, we examine the Wannier diagrams to identify the insulating states at charge neutrality. We establish the presence of three types of electronic states: moiré, mixed, and conventional. These states describe both the bulk Landau levels and the edge states crossing gaps in the spectrum. The evolution of the bulk moiré flat band wave functions in the magnetic field is investigated, predicting a decay of the electronic density from the moiré centers as the magnetic flux increases. Furthermore, the spatial properties of the three types of edge states are studied, illustrating the evolution of their localization as a function of the nanoribbon momentum.

I. INTRODUCTION

Stacking atomically thin materials with a relative twist or a mismatch of lattice constants leads to the system exhibiting superlattice periodicity due to the moiré interference between the layers. These moiré materials are intriguing physical systems where novel effects arise thanks to the high tunability of these structures, making them promising candidates for quantum simulators, especially given their capacity to access vastly different regimes of electronic matter via gate tuning. Recently, they have been an object of a great experimental [1–19] and theoretical interest [20–109].

In the case of magic-angle twisted bilayer graphene (MATBG), the moiré lattice potential leads to the formation of two flat energy bands, a valence and a conduction band, around charge neutrality. Due to the presence of spin, valley, and layer degrees of freedom in MATBG, there are multiple possibilities for ground states at partial filling of the flat bands counted in the number of electrons per moiré unit cell. The eight spinful flat bands are characterized using the filling fraction $\nu = [-4, 4]$, where $\nu = -4$ corresponds to completely empty flat bands and $\nu = 4$ to fully occupied bands. The interacting electrons occupying these bands

exhibit a variety of strongly correlated phases, allowing us to study the competition between interactions and topological effects. The correlated insulating states were initially observed [1] in the case of an integer number of particles per moiré unit cell, with superconductivity for noninteger fillings [2]. Since then, properties of MATBG have attracted immense experimental interest [1–9,11–19,89,110–138]. Substantial sample-to-sample variations and conflicting results show different ground states, which are perhaps close in energy and their energetic hierarchy is influenced by subtle details. Several factors, including hexagonal boron nitride (hBN) substrate alignment [117,123,139–150], strain physics [66,100,151], and twist angle disorder [8,97] have been suggested as potential contributors.

Current theoretical approaches to study MATBG include the continuum models [8,17,20,22–27,32,33,60,62,64–67], Hubbard-like lattice models [11,12,18,29,35–37,39,40,42,44,48,49,57,94,152], and heavy fermion description [81,153,154], which, however, cannot provide insight into the realistic edge states or atomistic defects in the sample. *Ab initio* or atomistic tight-binding calculations can tackle such issues, but they prove to be challenging due to the intrinsically large scale of the problem, i.e., a large number of atoms in a moiré unit cell for small twist angles. Some analysis of the edge states has been performed for the twisted bilayer graphene (TBG) at larger twist angles [155], and with an assumption of an enlarged interlayer hopping to simulate the behavior of MATBG [156,157].

*awaniaro@uottawa.ca
†maciej.bieniek@pwr.edu.pl

Recently, considerable effort has been put into studying the electronic properties of MATBG in a magnetic field. The intriguing aspect here lies in the comparable MATBG moiré and magnetic length scales for experimentally accessible magnetic fields. Focusing on the insulating states, a rich phase diagram in the magnetic flux versus the filling factor has been observed [6–9,13–17,19,110–127] in magnetotransport and local electronic compressibility measurements. Streda formula can be used to determine their topological properties [118,158]. However, if the observed insulating states are topologically trivial (have zero Chern number), it might happen that they originate, e.g., from a combination of two states with opposite Chern numbers. This can especially occur if there is no energy gap between the flat conduction and the flat valence bands. This energy gap can be opened by breaking the inversion and time reversal symmetry at a single particle level, which in practice is done by aligning MATBG sample with hBN [13,116–118].

For magnetic fields around 27 T, the entire flux quantum per moiré unit cell is already achieved [159] and physics related to the Hofstadter's fractal structure of the electronic gaps can be observed. Numerous aspects have already been elucidated through the effective models [25,151,154,159–179]. Initial studies concentrated on the general accessibility of the Hofstadter physics with experimentally available magnetic fields [155,159,180]. The topological aspects of the flat band Landau levels (LLs) have been analyzed [25,27,58,156,162–164,169,171,178] and the Hofstadter butterfly in the chiral limit has been studied in Refs. [166,170]. The physics of flat bands in strong magnetic field and possible reentrant superconductivity have been addressed [173,174,178,179,181]. The atomistic tight-binding calculations of TBG were able to confirm the effective model results in the large magnetic field regime as well as provide insight into the edge states. These calculations mainly focus on larger twist angles, which result in a smaller moiré unit cell [180–183]. To investigate the electronic properties of MATBG at the atomistic scale, a large sample is needed (~1 μm), simulating which involves costly computation.

Our multimillion-atom simulation sheds light on the MATBG's on top of hBN in a magnetic field behavior within experimentally feasible scenarios. We consider realistic sample sizes consisting of up to 1 000 000 atoms, allowing us to relate the obtained Hofstadter spectrum to the experimental observations and gain insight into the microscopic properties of the wave functions for both bulk and edge states. This establishes a solid foundation for future investigations of the magnetic phase diagram, incorporating both magnetic fields and electron-electron interactions.

The paper is organized as follows. In Sec. II, we introduce an atomistic model of TBG, define a unit cell for commensurate twist angles and nanoribbon geometries, and describe an *ab initio*-based tight-binding model. Then we proceed to present our theoretical framework for investigating the electronic properties of MATBG under the influence of a magnetic field. Section III is devoted to the study of the electronic structure of MATBG. In the remaining sections, we focus on MATBG in the nanoribbon geometry and begin our analysis in Sec. IV studying the size effects in the electronic structure. We subsequently introduce the effect of the magnetic field
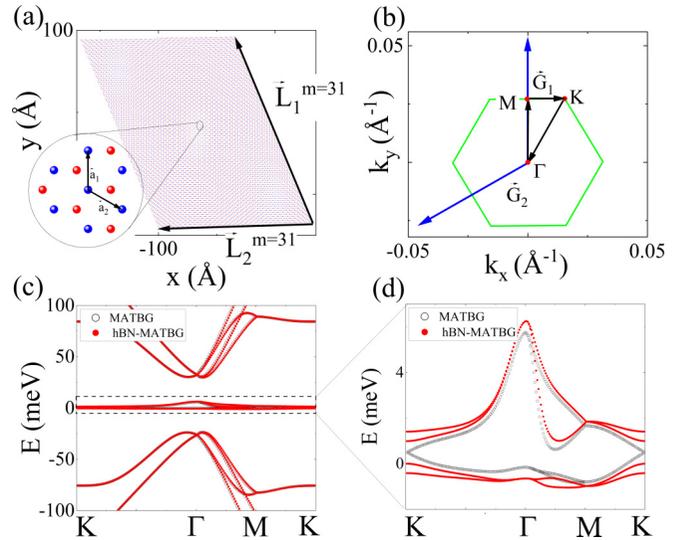
FIG. 1. Structural and electronic properties of moiré lattice. (a) Moiré unit cell for MATBG consisting of 11 908 atoms, spanned by the superlattice vectors $\vec{L}_1$ and $\vec{L}_2$. The inset provides a zoom-in on a graphene structure with A and B atoms denoted by blue and red dots. The primitive lattice vectors $\vec{a}_1$ and $\vec{a}_2$ are also indicated. (b) Moiré BZ defined by the reciprocal lattice vectors $\vec{G}_1$ and $\vec{G}_2$. (c) MATBG band structure within a 200 meV energy window along the K-Γ-M-K path marked in (b). MATBG is represented by black circles, while the dispersion for MATBG on an hBN substrate is illustrated by red dots. (d) A corresponding zoom-in on the flat band.

in Sec. IV A, where we present the results in the form of a Hofstadter spectrum. This spectrum forms the basis for the construction of Wannier diagrams, as discussed in Sec. IV B. Turning our focus to microscopic properties, Sec. IV C examines the bulk and edge wave functions. Here, we identify three distinct types of states, namely, the conventional, moiré, and mixed states. Concluding our analysis, Sec. IV D provides an analysis of bulk and edge states, studying their evolution as a function of the magnetic field and nanoribbon 1D momentum.

II. MODEL AND THEORETICAL METHODS

A. Structural properties of twisted bilayer graphene

Graphene is composed of carbon atoms arranged on a honeycomb lattice with two atoms, A and B, inside a unit cell. The primitive lattice vectors are defined as $\vec{a}_1 = (0, \sqrt{3}a)$ and $\vec{a}_2 = (3a/2, -\sqrt{3}a/2)$, where $a = 1.412$ Å represents the carbon-carbon distance, see Fig. 1(a). TBG is defined as two graphene sheets in a Bernal stacking, rotated by an angle θ around the (0,0) point. If θ belongs to a set of commensurate twist angles, the structure exhibiting moiré periodicity and linearly independent moiré primitive vectors can be defined as follows:

$$\vec{L}_1^{(m)} = m\vec{a}_1 - (m+1)\vec{a}_2,$$
$$\vec{L}_2^{(m)} = -(m+1)\vec{a}_1 - (2m+1)\vec{a}_2. \quad (1)$$

m is an integer, which can be used to define θ in following the formula [21]: $\cos(\theta_m) = (3m^2 + 3m + 1/2)/(3m^2 + 3m + 1)$.

We focus on the magic angle $\theta = 1.05°$, which corresponds to $m = 31$. The number of atoms within a moiré unit cell can be calculated through the relation $N_{at} = 4(m^2 + (m+1)^2 + m(m+1))$, which, for the magic angle, yields $N_{at} = 11\,908$ atoms.

The distance between the two graphene layers depends on the relative stacking and is nonuniform in the moiré unit cell. We account for the lattice relaxation effects along the z axis by varying the interlayer distance based on the stacking configuration. The layers are closest to each other in the AB-stacked regions where $z_{AB} = z_{min} = 3.34$ Å. The largest distance arises in AA stackings, for which we adopt $z_{AA} = z_{max} = 3.61$ Å [184]. To determine the relaxed interlayer distance z_{relax}, we introduce a stacking parameter δz assigned to each atom. This parameter depends on the distance in the xy plane between the considered atom and its nearest neighbor of a different type in the other layer. Specifically, it is defined as $\delta z = a^{-1}\sqrt{(x_1 - x_2)^2 + (y_1 - y_2)^2}$, where x_1 and y_1 describe the position of the considered atom, and x_2 and y_2 refer to its nearest neighbor in the other layer. The factor a^{-1} is included, so $\delta z = 0$ in the AA stacking and $\delta z = 1$ for the AB stacking. The relaxed interlayer distance is then calculated as $z_{relaxed} = z_{max} - \delta z(z_{max} - z_{min})$.

Using the superlattice vectors $\vec{L}_1$ and $\vec{L}_2$, we determine the corresponding reciprocal space primitive vectors $\vec{G}_1$ and $\vec{G}_2$, which are used to construct a moiré Brillouin zone (BZ). Using the definition $\vec{G}_i \cdot \vec{L}_j = 2\pi \cdot \delta_{ij}$, we derive $\vec{G}_1$ and $\vec{G}_2$ in the form

$$\vec{G}_1 = \left[-\frac{2\pi}{3a}\frac{1}{3m^2 + 3m + 1}, \frac{2\pi}{3a}\frac{\sqrt{3}(2m+1)}{3m^2 + 3m + 1} \right],$$

$$\vec{G}_2 = \left[-\frac{2\pi}{3a}\frac{3m+1}{3m^2 + 3m + 1}, \frac{2\pi}{3a}\frac{\sqrt{3}(m+1)}{3m^2 + 3m + 1} \right]. \quad (2)$$

After obtaining $\vec{G}_1$ and $\vec{G}_2$, we proceed to construct a moiré BZ, in which high-symmetry points Γ, K, M can be identified, as illustrated in Fig. 1(b).

To study the effects of a magnetic field, we construct a nanoribbon structure by stacking moiré unit cells in the $\vec{L}_1$ direction and applying periodic boundary conditions in the $\vec{L}_2$ direction. We analyze nanoribbons composed of up to 85 moiré unit cells, which means that we simulate MATBG system widths of up to 10^6 atoms in the direction perpendicular to the periodicity. For consistent detection of the edge and bulk states, we define the edge as encompassing 10% of the ribbon's width at both the lower and upper ends of the sample. The remaining 80% of atoms constitute the bulk region of the structure. To manage the computational effort of diagonalizing matrices of such dimensions, we have used the high-performance FEAST algorithm [185], which offers enhanced efficiency in the computation of the eigenvalues within a designated energy interval.

The choice of a moiré unit cell for an infinite system is, in general, arbitrary with respect to the real-space coordinate system. However, due to our finite geometry, each particular definition of the unit cell has consequences for the electronic properties of our system. To avoid cutting through the AA region, where the flat band LDOS is expected to localize, we have chosen a unit cell that centers around the AA-stacked atoms and maximizes the region of the moiré center. This is achieved by shifting the unit cell by $(\vec{L}_1 + \vec{L}_2)/6$ with respect to the AB-stacked atoms at the coordinates $(0,0)$. By doing so, we have created an irregular edge which affects the properties of our system on the order of 0.1 meV. This effect is visible, for example, in the flat band of large nanoribbons where the states shift with respect to the band edges deduced from the infinite system.

B. Tight-binding model in magnetic field

We employ an *ab initio*-based tight-binding model for p_z atomic orbitals [128,186] and tunneling over all the atoms in the sample, with a Hamiltonian given by

$$\hat{H}_{TB} = \sum_{i,j}^{N} \sum_{\sigma} t(\vec{r}_i, \vec{r}_j)(c_{i,\sigma}^\dagger c_{j,\sigma} + c_{j,\sigma}^\dagger c_{i,\sigma}). \quad (3)$$

$N = N_{UC}N_{at}$ represents the total number of atoms equal to the number of unit cells multiplied by the number of atoms in the unit cell, while $c_{i,\sigma}^\dagger$ ($c_{i,\sigma}$) is the creation (annihilation) operator on the ith site located at the coordinate $\vec{r}_i = (x_i, y_i, z_i)$ with spin $\sigma = \{\uparrow, \downarrow\}$. The out-of-plane coordinate z_i is given by its relaxed value $z_{relaxed}$. The hopping term is defined as [186]

$$t(\vec{r}_i, \vec{r}_j) = (1 - n^2)\gamma_0 \exp\left(\lambda_1\left(1 - \frac{|\vec{r}_i - \vec{r}_j|}{a}\right)\right)$$
$$+ n^2\gamma_1 \exp\left(\lambda_2\left(1 - \frac{|\vec{r}_i - \vec{r}_j|}{c}\right)\right), \quad (4)$$

where $a = 1.412$ Å is again the carbon-carbon distance, and $c = 3.36$ Å is a unrelaxed interlayer distance. The direction cosine along the z axis is denoted by n. Intralayer hopping is parametrized by $\gamma_0 = -2.835$ eV, and interlayer by $\gamma_1 = 0.48$ eV. The dimensionless decay constants are $\lambda_1 = 3.15$ and $\lambda_2 = 7.50$. These parameters were obtained by the fitting to the *ab initio* results of unrotated graphene bilayer in different stacking configurations, as well as bilayers rotated by larger twist angles. A general solution for all twist angles has been interpolated from these calculations. These parameters are known to reproduce well the *ab initio* band structure of MATBG [128,187], as well as the *ab initio* Dirac cone velocity renormalization for arbitrary twist angles [186]. We opt for $\gamma_0 = -2.835$ eV value to match our band structure as well as possible the state-of-the-art *ab initio* MATBG band structure in Ref. [187], focusing on flat band width, remote band gaps values, and electron-hole asymmetry in the flat band. For our calculations, we consider interactions of atoms within a distance $\leqslant 6a$ from the considered atom. Including additional neighbors does not cause significant quantitative changes in our results. For example, if the cutoff radius is set to $r_{cutoff} = 7a$, maximal flat band energy difference is 0.002 meV around Γ point in the top conduction band of the flat band. However, for a smaller hopping radius (e.g., $r_{cutoff} = 4a$), the band-structure difference becomes visible, e.g., of the order of 0.5 meV around the Γ point for the flat band and conduction band. To account for the presence of an hBN substrate, we introduce a staggered potential $\Delta = 10$ meV to the bottom layer of our system [188,189]. To include this in our Hamiltonian, we add a diagonal part $H_{hBN} = \sum_{i,\sigma} \Delta_i c_{i,\sigma}^\dagger c_{i,\sigma}$, where $\Delta_i = 5$ meV if i belongs to the set of A atoms, and

$\Delta_i = -5$ meV if i belongs to the set of B atoms. If i belongs to the set of atoms from the top layer, $\Delta_i = 0$ meV.

As we have already mentioned, each moiré unit cell consists of N_{at} number of atoms. Each atom repeats in the unit cells creating N_{at} simple Bravais sublattices. For a given wave vector $\vec{k}$ for each sublattice n, we can define a wave function:

$$\Psi_{\vec{k}}^n = \frac{1}{\sqrt{N_{UC}}} \sum_\alpha^{N_{UC}} e^{i\vec{k}\cdot(\vec{\tau}_n + \vec{R}_\alpha)} \phi_z(\vec{r} - \vec{\tau}_n - \vec{R}_\alpha). \quad (5)$$

Here, $\vec{\tau}_n$ refers to the position of an atom within a unit cell, while $\vec{R}_\alpha$ denotes the position of different unit cells. To construct our Hamiltonian in the second quantization, we expand the field operators in sublattice wave functions for each wave vector $\vec{k}$, e.g., $\hat{\Psi}_{\vec{k}}^\dagger = \sum_n^{N_{at}} \sum_\sigma c_{\vec{k},n,\sigma}^\dagger \Psi_{\vec{k}}^{*n}$. Here $c_{\vec{k},n,\sigma}^\dagger$ $(c_{\vec{k},n,\sigma})$ are the creation (annihilation) operators that create (annihilate) particles with momentum $\vec{k}$ on sublattice n and spin σ. We can now define an $\hat{H}_k$ operator for each considered $\vec{k}$ value:

$$\hat{H}_{\vec{k}} = \int dr \hat{\Psi}_{\vec{k}}^\dagger H \hat{\Psi}_{\vec{k}} = \sum_{n,m=1}^{N_{at}} \sum_\sigma c_{\vec{k},n,\sigma}^\dagger c_{\vec{k},m,\sigma} \int dr \Psi_{\vec{k}}^{*n} H \Psi_{\vec{k}}^m. \quad (6)$$

We introduce $H_{\vec{k}}^{nm} = \int dr \Psi_{\vec{k}}^{*n} H \Psi_{\vec{k}}^m$ as a matrix in the space of sublattices which has the form

$$H_{\vec{k}}^{nm} = \int dr \left[\frac{1}{\sqrt{N_{UC}}} \sum_\alpha^{N_{UC}} e^{-i\vec{k}\cdot(\vec{\tau}_n + \vec{R}_\alpha)} \phi_z^*(\vec{r} - \vec{\tau}_n - \vec{R}_\alpha) \right]$$
$$\times H \left[\frac{1}{\sqrt{N_{UC}}} \sum_\beta^{N_{UC}} e^{-i\vec{k}\cdot(\vec{\tau}_m + \vec{R}_\beta)} \phi_z(\vec{r} - \vec{\tau}_m - \vec{R}_\beta) \right]. \quad (7)$$

Now we center our system at $\vec{r}' = \vec{r} - \vec{\tau}_n - \vec{R}_\alpha$ and define $\vec{R}_\gamma = \vec{R}_\alpha - \vec{R}_\beta$. These operations lead us to a simplified expression:

$$H_{\vec{k}}^{nm} = \frac{1}{N_{UC}} \sum_\alpha^{N_{UC}} \sum_\gamma^{N_{UC}} e^{-i\vec{k}\cdot(\vec{\tau}_n - \vec{\tau}_m)} e^{-i\vec{k}\vec{R}_\gamma}$$
$$\times \int dr \phi_z^*(\vec{r}) H \phi_z(\vec{r} + \vec{\tau}_n - \vec{\tau}_m + \vec{R}_\gamma). \quad (8)$$

Defining $t(\vec{\tau}_n, \vec{\tau}_m + \vec{R}_\gamma) = \int dr \phi_z^*(\vec{r}) H \phi_z(\vec{r} + \vec{\tau}_n - \vec{\tau}_m + \vec{R}_\gamma)$, we can write our final form:

$$H_{\vec{k}}^{nm} = \sum_\gamma^{N_{UC}} e^{-i\vec{k}\cdot(\vec{\tau}_n - \vec{\tau}_m)} e^{-i\vec{k}\vec{R}_\gamma} t(\vec{\tau}_n, \vec{\tau}_m + \vec{R}_\gamma). \quad (9)$$

We note that because the hopping vanishes quickly with the distance, the sum over γ reduces to a single nonzero element from either the considered unit cell or its nearest neighbors. Hopping terms $t(\vec{\tau}_n, \vec{\tau}_m + \vec{R}_\gamma)$ are defined in Eq. (4) and depend on the sublattice and unit cell position of the considered atoms. $\vec{k} = (k_x, k_y)$ represents the wave vector within the first moiré BZ.

In a nanoribbon structure, we incorporate the periodicity solely in the x direction, modifying our Hamiltonian to have the form

$$\hat{H}_{k_{1D}} = \sum_{n,m}^{N_{at}} \sum_\sigma c_{k_{1D},n,\sigma}^\dagger c_{k_{1D},m,\sigma} H_{k_{1D}}^{nm}, \quad (10)$$

where $k_{1D} \in (-\pi/|\vec{L}_2|, \pi/|\vec{L}_2|)$ denotes the wave vector in the one-dimensional BZ of the ribbon.

Thanks to the nanoribbon geometry, perpendicular magnetic field can be introduced using Peierls substitution in the Landau gauge $\vec{B} = \vec{\nabla} \times \vec{A}$, with vector potential $\vec{A} = (-B_z y, 0, 0)$:

$$\tilde{t}(\vec{r}_i, \vec{r}_j) = t(\vec{r}_i, \vec{r}_j)^{B_z=0} \exp\left(-i\pi \frac{2eB_z}{hc} \frac{(x_j - x_i)}{2} (y_i + y_j) \right). \quad (11)$$

Here $hc/2e$ is the magnetic flux quantum φ_0. The Zeeman splitting is included by adding a diagonal part to our Hamiltonian in the form $H_Z = \frac{1}{2} g \mu_B B_z \sum_i (c_{i,\uparrow}^\dagger c_{i,\uparrow} - c_{i,\downarrow}^\dagger c_{i,\downarrow})$, where μ_B is the Bohr magneton and g is the Landé factor. To use the Landau gauge, we perform a global rotation of the coordinate system, ensuring strict x-axis periodicity. Due to such periodicity, we are able to include a magnetic field in our nanoribbons without the restriction to specific magnetic flux values.

We note the existence of the topologically trivial and nontrivial edge states characterized by Chern numbers. The Chern numbers are determined by counting the number of chiral edge states crossing the energy gap. The microscopic properties of the wave functions of the flat band and the edge states are characterized by the local density of states (LDOS) for a representative choice of the magnetic field. We use the following definition of LDOS:

$$n(x_i, y_i, E) = N_{k_{1D}}^{-1} \sum_{\lambda, k_{1D}} |\psi_{k_{1D}, \lambda}(x_i, y_i)|^2 \delta(E - E_{k_{1D}, \lambda}). \quad (12)$$

Here, n is the LDOS for given coordinates x_i and y_i in a chosen energy window. $N_{k_{1D}}$ is the normalization constant and relates to the number of states considered, λ is the eigenvalue index, which together with the wave vector k_{1D} enumerates the eigenvalue $E_{k_{1D}, \lambda}$ and the eigenvector $\psi_{k_{1D}, \lambda}(x_i, y_i)$.

C. Wannier diagrams

To establish a connection between the Hofstadter spectrum and the experimental observations, Wannier diagrams can be used [190]. These diagrams can be constructed by plotting the integrated charge carrier density, up to a given energy level, versus the magnetic field B. This representation highlights the linear trends in energy gaps, offering a useful representation of electronic gaps in the Hofstadter-like spectrum, encompassing both single-particle and many-body interaction-induced Mott-like gaps. Moreover, linear fitting of the data in the Wannier diagrams aids in identifying unconventional states that defy a simple LL picture and related single-particle Chern insulators. Such unconventional ground-state sequences have been recently observed [117,123] and explained by the sequential flavor filling mechanism. Wannier plots obtained by mapping these gaps as functions of filling and magnetic field provide a direct comparison with the compressibility and transport
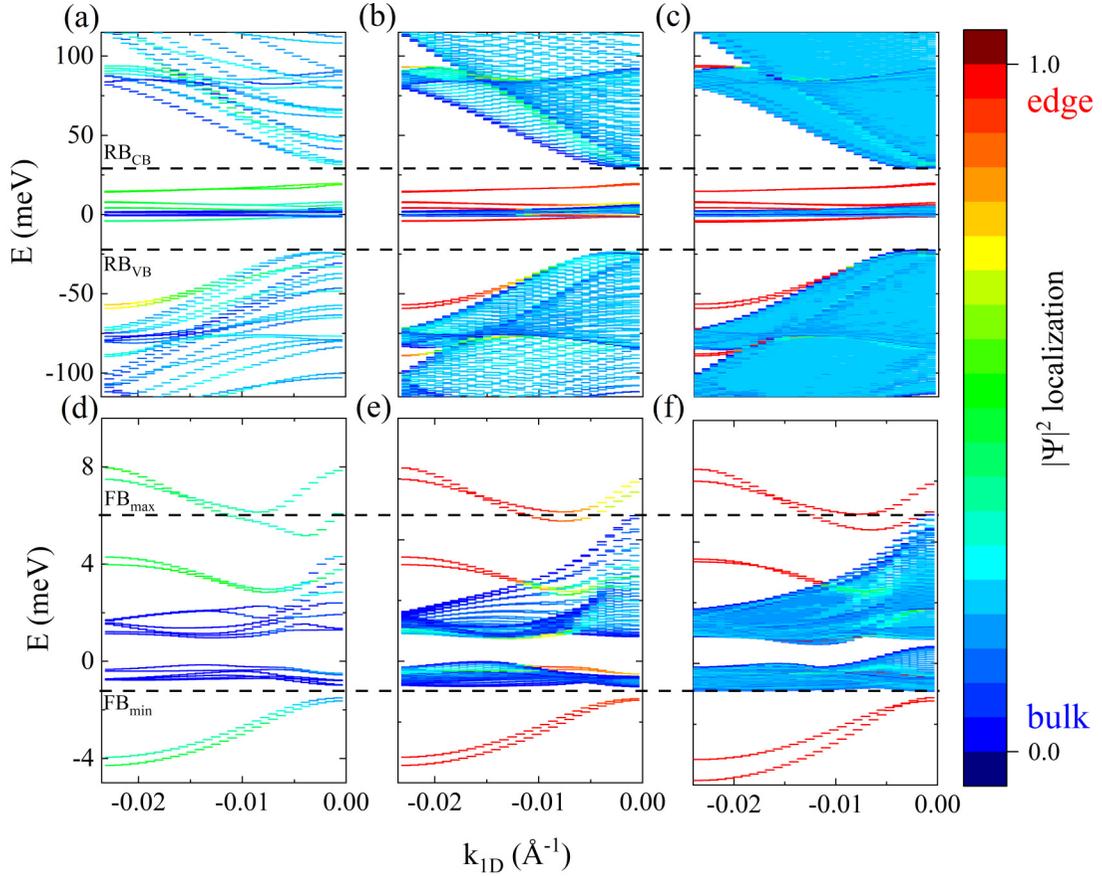
FIG. 2. The electronic structure of the MATBG ribbon on an hBN substrate revealing quantization effects for the flat and remote bands. (a)–(c) in the top panels show bands within a 200 meV energy window for different ribbon widths: (a) 5, (b) 20, and (c) 85 moiré unit cells. (d)–(f) The lower panels provide a zoom into the flat band for analogical nanoribbon widths. Color coding signifies the localization of states in real space. The dashed lines represent band edges that are deduced from the infinite system calculations. RB_{CB} (RB_{VB}) refers to the top (bottom) of the remote conduction (valence) band, while FB_{max} (FB_{min}) marks the top (bottom) of the flat band.

experiments [15,17,110,115–118,123] and can serve as a tool for identifying (non)interacting insulating states.

III. ELECTRONIC STRUCTURE OF TWISTED BILAYER GRAPHENE

In Figs. 1(c) and 1(d), we present the band structure of MATBG along the K-Γ-M-K line. In Fig. 1(c), we display the energy window that captures the flat band and the remote valence and conduction bands. In our model, we find the flat band that is 7 meV wide and separated by a 25 meV gap from the remote bands. These values are in a good agreement with other tight-binding models [191] as well as with the density functional theory calculation [184,187,191,192]. Achieving such results became possible only after incorporating the out-of-plane relaxation effects, which led to the enlargement of the band gaps, as well as widening of the flat band compared to the ideally flat MATBG. Notably, our model inherently lacks electron-hole symmetry. This feature contrasts with the continuum, Bistritzer-MacDonald model, where electron-hole asymmetry is obtained by adding momentum dependent interlayer scattering terms [193].

In Fig. 1, we demonstrate the influence of the hBN substrate on the MATBG dispersion. In Fig. 1(c), the black circles

represent a pristine MATBG sample, while the red dots denote the system on the substrate. One can notice that the presence of hBN has a negligible effect on the higher energy spectrum (i.e., remote bands) and the band gaps between the flat band and the remote bands remain unchanged. The impact of hBN becomes more apparent if we focus on the flat band, see Fig. 1(d). In this context, the presence of hBN leads to the opening of the gap at K points and splitting of the degeneracies.

IV. QUANTUM SIZE EFFECTS IN ELECTRONIC STRUCTURE OF TWISTED BILAYER GRAPHENE

The electronic structure of the MATBG nanoribbons on an hBN substrate, considering various system widths, is analyzed in Fig. 2, where we plot the energy subbands as a function of the one-dimensional momentum k_{1D}. In Figs. 2(a)–2(c), bands in 200 meV energy window are shown, while Figs. 2(d)–2(f) provide a close-up view of the flat band. The color scale corresponds to the localization of the wave function. States localized on either of the sample's edges are represented in red, while bulk states that lie closer to the center of the system are displayed in blue. Given the symmetry of the spectrum with respect to $k_{1D} = 0$, only half of it is depicted. Dashed
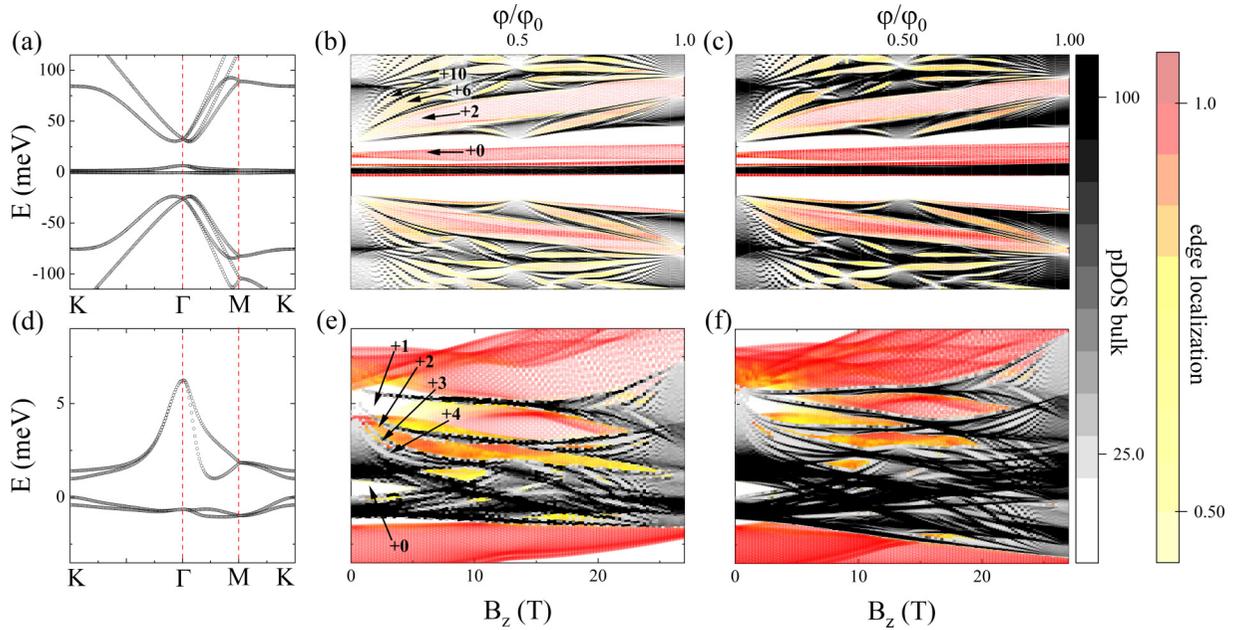
FIG. 3. The band structure and Hofstadter spectrum of a MATBG ribbon on an hBN substrate. (a) Flat and remote bands within an approximately 200 meV energy window around the Fermi level along the K-Γ-M-K line on the moiré Brillouin zone. (b) The Hofstadter spectrum for magnetic flux $\varphi/\varphi_0 = [0, 1]$, corresponding to magnetic field $B_z \approx [0, 27]$ T. This data is obtained from the nanoribbon density of states. The data points shown in grayscale represent projected density of states of the bulk, while the edge states are visualized in color. (c) Similar Hofstadter spectrum with Zeeman splitting included. The zoom-in to the energy window $E = [-5, 10]$ meV of the flat band is shown in (d)–(f). Arrows highlight the gaps that we characterize by the in-gap Chern numbers.

lines denote the band edges inferred from the band structure of the 2D infinite system. In the case of the smallest system consisting of five moiré unit cells, as depicted in Figs. 2(a) and 2(d), the bulk states are predominant and no edge states are apparent due to their strong hybridization with the bulk states. As the system size increases, edge states become more evident, clearly visible as red lines in Figs. 2(b) and 2(e). This feature becomes even more pronounced for wider ribbons with band structures, shown in Figs. 2(c) and 2(f). We note that the wave function localization observed for the case of 20 moiré unit cells is in good agreement with the results for 85 moiré unit cells. Given the constant number of the edge states, the bulk band edges together with the gap widths, we have opted to use the system consisting of 20 moiré unit cells in the subsequent calculations. We note that in Appendix A we confirmed the applicability of our method to study the edge effects by reproducing the moiré flat-band breakdown shown recently in experiment in Ref. [194].

We also note two interesting features apparent at this stage of analysis. First, there exists a distinct band gap around $E = 0$ meV in all three cases, arising due to the presence of an hBN substrate. In the gap region, no edge states link the bulk states above and below, resulting in a trivial gap with a Chern number $C = 0$ [195]. Second, we examined the flat subband degeneracy, which is constant for every wave vector k in the energy window between the remote bands. The number of states is always equal to the product of the moiré nanoribbon unit cell number and 8 (representing two bands, two valleys, and two spins). This way there are always 20 states for each k and each spin in Fig. 2(a), 80 in Fig. 2(e), and 340 in Fig. 2(f). This total number of states encompasses both edge and bulk

states, however, the number of edge states remains constant regardless of the ribbon width. This observation implies that the two trivial edge states running below and the four states running above the flat band must originate from the flat-band states.

A. Moiré-Hofstadter spectrum

We analyze the influence of the perpendicular magnetic field on MATBG on top of hBN, exploring several aspects of the fractal spectrum. We consider magnetic fields in the range $\varphi/\varphi_0 = [0, 1]$, corresponding to approximately $B_z \approx [0, 27]$ T. We note that the size study in nonzero magnetic field has been conducted for nanoribbons consisting of up to 85 moiré unit cells. Similar to the case of $B_z = 0$ T, a nanoribbon consisting of 20 moiré unit cells remains representative of the larger structures. The resulting Hofstadter spectrum is displayed in Fig. 3, with a clear repeated pattern of energy gaps at different energy scales. Since our calculations are performed for a nanoribbon geometry, both bulk and edge states are present. The grayscale refers to the projected density of the bulk states, while the color scale indicates the degree of localization of the edge states. In Fig. 3(b), we show the fractal spectrum without the effect of the Zeeman splitting. First, we confirm that the width of the overall flat band remains constant and the flat bands do not mix with the remote bands up to one flux. From the remote bands, one can clearly observe the formation of the LLs for magnetic field $B_z < 5$ T and their evolution as a function of B_z. Flat energy band along M-K path around 80 meV and -80 meV without a magnetic field translates into the van Hove singularities that seem to
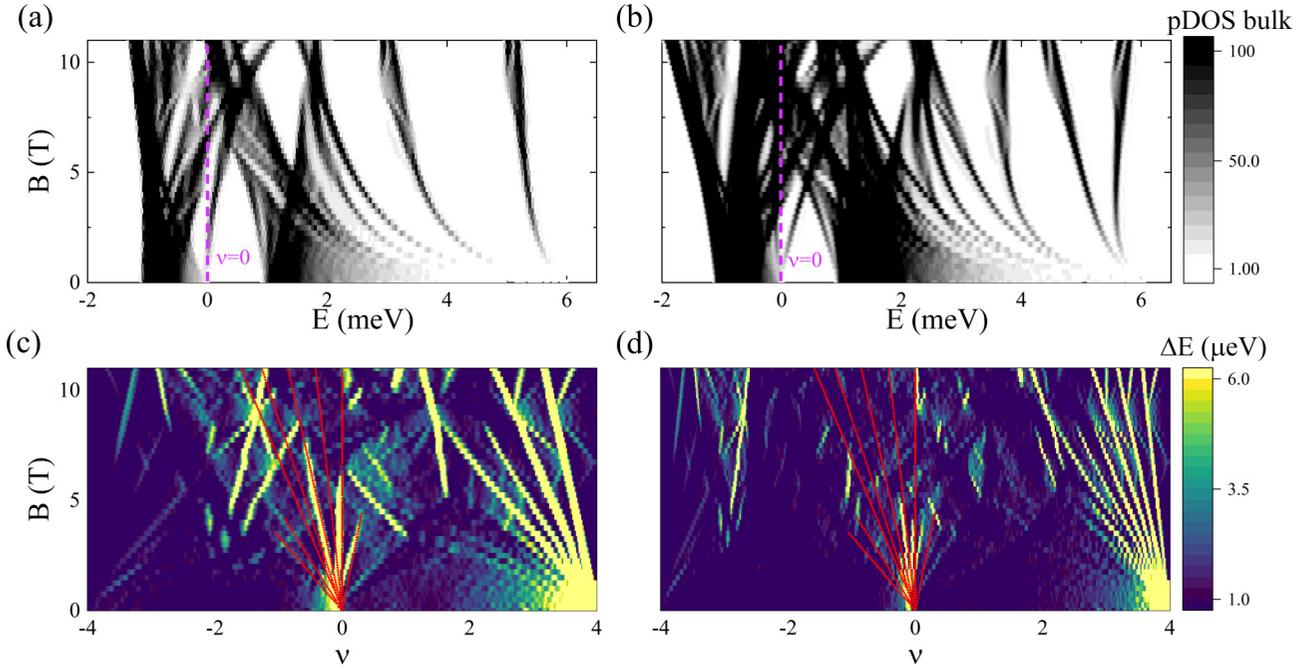
FIG. 4. Wannier diagram of the hBN-MATBG ribbon flat band in the presence of a magnetic field. (a) Hofstadter spectrum for the bulk states of the flat band, extracted from data presented in Fig. 1(d). (b) Hofstadter spectrum including Zeeman splitting. (c) Wannier diagram corresponding to the spectrum in (a). The x axis measures the filling ν relative to the Fermi level. Filling -4 (4) indicates a completely empty (filled) flat band. The color scale is used to denote the energetic width of the band gaps ΔE. Note that all gaps larger than 6 μeV are denoted by the same color. (d) Like (c), but this Wannier diagram is derived from the Hofstadter spectrum with Zeeman splitting included. The red dotted lines on (c) and (d) mark some of the gaps starting at $\nu = 0$ extracted from the experimental data [117]. All panels (a)–(d) have the same y axis, denoting the magnetic field $B_z = [0, 11]$ T.

be unaffected by small magnetic fields $B_z < 5$ T. There are no crossings of the edge state between the flat and remote bands, which leads to the conclusion that both of these gaps are trivial, and the in-gap Chern number is $C = 0$. Analyzing the edge states crossing between the other LLs, we determine the in-gap Chern numbers for the other cases. The results of the edge state counting are marked with arrows pointing to the specific gaps. In Fig. 3(c), we present an analogical spectrum including the effect of the Zeeman splitting $E = \pm \frac{1}{2} g \mu_B B_z$. In this energetic scale, the only visible effect is a small broadening of the LLs, since the Zeeman splitting energy is of the order $\sim 10^{-2}$ meV/T.

In Figs. 3(e) and 3(f), we present close-ups of the Hofstadter spectra around the Fermi level, focusing on a flat band region, once again with and without the Zeeman splitting, respectively. We analyze the in-gap Chern numbers corresponding to the number of edge states crossing it, concluding that the gap opened by hBN has no edge states crossing through it and is, therefore, trivial with $C = 0$. The band gaps within the split conduction band exhibit a sequence of Chern numbers: $C = 1$, followed by $C = 2$, $C = 3$, and $C = 4$. Notably, the top of the conduction band near the Γ point has a negative effective mass, leading to the highest flat-band LL, decreasing in energy for an increasing magnetic field. This tendency deepens when we incorporate the Zeeman splitting, as seen in Fig. 3(f). In the case of the flat band, the Zeeman term corrections lead to the broadening of the energy bands related to the splitting of the Hofstadter spectrum.

B. Analysis of Wannier diagrams

Through the analysis of the Hofstadter spectrum, a Wannier diagram can be obtained, as described in Sec. II C. For clarity, we first repeat our Hofstadter spectra, choosing a smaller magnetic field range in Figs. 4(a) and 4(b). Note that now the magnetic field B_z is plotted on the y axis. We focus on the flat band and extract only the bulk projected density of states. In Figs. 4(a) and 4(b), we show the Hofstadter spectra without and with the Zeeman term, respectively.

The width of the energy gaps within the flat band is depicted in color in Figs. 4(c) and 4(d) as a function of the filling ν and magnetic field B_z. The red dotted lines mark some of the gaps that can be observed in the compressibility experiments [117]. Comparing this single-particle result with the experimental data provides a direct means of identifying noninteracting, insulating states. We have achieved good agreement with the experiment for fillings around $\nu = 0$ and low magnetic fields. This suggests qualitatively correct mean-field, *ab initio*-based tight-binding picture around charge neutrality; correlations do not play an important role here. On the downside, the vertical line at $\nu = 0$, representing the largest electronic gap in the flat band spectrum, vanishes around $B_z = 5$ T, whereas in the experiments this gap remains open over the entire 0–11 T magnetic field range, see also Fig. 2 in Ref. [117] for comparison. When the Zeeman splitting is included in our calculations, as shown in Fig. 4(d), some of the gaps have shifted to odd integer fillings, leading to better agreement with the experimental results, e.g., the gaps

visible in Fig. 4(c) around $\nu = -2$ for $B_z > 3$ T have shifted to $\nu = -3$ also for $B_z > 3$ T. However, since the number of gaps has doubled and their widths have decreased, some of the previously prominent features have become less distinct, e.g., note the rightmost gap beginning at $\nu = 0$ and closing around $B_z = 5$ T. It is well visible in Fig. 4(c) in agreement with the experimental data, but becomes much less clear after including the Zeeman splitting, see Fig. 4(d). Hence, studying both scenarios—with and without the Zeeman splitting—can provide valuable insights and enable us to better determine which gaps are not related to the effects of interaction. While we leave the electrostatic and many-body interactions for future work, we anticipate a widening of the gaps around integer fillings. Moreover, there is a very strong feature below $\nu = 4$ stemming from the well-separated top flat-band LL, which is not observed in the experiments. This suggests a significant renormalization beyond the current understanding of the energy dispersion around the Γ point in the magnetic field due to the presence of interactions or magnetic fields.

C. Conventional, mixed, and moiré state properties

Within an energy window of approximately 100 meV around charge neutrality, two types of bulk magnetic bands with highly suppressed kinetic energy emerge. The first are the moiré flat bands, which in the real-space picture correspond to states mostly localized in the AA-stacked regions [20] of the twisted bilayers. The second features more conventional LLs, which generally extend across the entire moiré unit cell and are not restricted to the moiré centers. It is currently unclear how these two types can be modeled simultaneously in low-energy theories and how they are mutually influenced. For example, several works show different behaviors of the Hofstadter butterflies and related different Chern numbers of the gaps [159,163,180,181]. Even less is known about the microscopic properties of wave functions of these levels, especially about chiral states connecting bulk bands, localized on the edges of TBG samples. Since this knowledge is crucial for understanding the topological aspects of MATBG, the interacting problem, Chern insulator states, potential reentrant superconductivity, and quantum geometric properties, [173,174,178,179,181,196] in our paper we provide general microscopic features of both bulk and edge states of MATBG in a magnetic field.

It is important to experimentally probe the edge-state physics, e.g., extend scanning tunneling spectroscopy studies of the breakdown of the moiré flat bands [194] to the identification of the Chern-moiré edge states, and extend transport studies of possible zero-field Chern phase [13] to nonlocal Hall measurements and to a finite magnetic field. The local probing of competing ground-state wave functions is still in its early stages for both experimental [197] and theoretical investigations [84,85].

Other exciting avenues for probing edge currents are superconducting quantum interferometry [198] and electron spin resonance edge probes [89,199–201]. Although some works have discussed the moiré edge states [50,156,180,195,202], they primarily centered on the effective models or twist angles greater than the magic angle. Studies using large-scale atomistic tight-binding models [93,94,186,203–210]

have predominantly focused on the electronic structures, relaxation effects, and interactions, serving as a basis for the construction of low-energy models.

Here we investigate the microscopic properties of the MATBG wave functions in a magnetic field for the 20 moiré unit cells nanoribbon and a representative magnetic field $B_z = 4$ T. The 1D band structure is shown in Figs. 5(a) and 5(b). We consider two energy windows, with $\Delta E \approx 150$ meV in Fig. 5(a), followed by a zoomed-in view of the flat band region ($\Delta E \approx 10$ meV) in Fig. 5(b). In both cases, we classify the ribbon states according to their localization. States colored in green represent the ones localized within the center of the sample, while states colored in red and blue correspond to those localized on the top or bottom edges, respectively. The bulk states form flat bands, i.e., the ribbon LLs, between some of which the edge-localized states cross the gaps. This is a characteristic signature of nonzero Chern number. We note that not all gaps are crossed by the states connecting bulk bands, suggesting the existence of trivial edge states.

Before we delve into the details of the real-space properties of the ribbon states, let us precisely define the meanings of conventional-, moiré-, and mixed-type states, classifications we use in the subsequent paragraphs. We label states as conventional if the LDOS is uniformly spread over the sample and resembles a typical LL distribution. Moiré states are characterized by the LDOS primarily concentrated around the moiré centers. For mixed states, LDOS is neither concentrated only around the moiré centers nor uniformly spread across the sample.

To analyze the real-space properties of the ribbon states, we have chosen three bulk LLs: the flat band (LL0) around $E = 0$ meV, the first LL (LL1) around $E = 30$ meV, and the second LL (LL2) around $E = 60$ meV. Our investigation of the microscopic properties of the electronic charge densities is summarized in Fig. 5(c), which shows the LDOS calculation and its spatial distribution. Within this analysis, we focus on three consecutive LLs, which represent three different types of bulk states. The first stripe shows the flat band, LL0, which, as expected, is a moiré-type state—the LDOS is concentrated predominantly around the region of the AA stacking in the real space. The second type, LL1, which is separated by a ~ 30 meV gap from the flat band, still strongly feels the LL0 influence, and also exhibits LDOS concentration around the moiré centers. This result is surprising, since LL1 is a regular LL and, in principle, should present a uniform spread of the wave function. The fact that it doesn't suggests a stronger influence from the flat band than anticipated, potentially observable in a broader energy range. This is an example of a mixed state. Moving to LL2, the conventional bulk state, we observe a more uniform LDOS spread, as one would expect. However, there is also an opposite trend present: LDOS avoids the moiré centers; note the yellow dots in the center of moiré unit cells for LL2 in Fig. 5(c). For higher LLs, the pattern is similar to that of LL2, with an even more evenly distributed wave function. A similar analysis can be conducted for the edge states. Once again, we identify three distinct types of edge states. Those states are indicated in Figs. 5(a) and 5(b) by E0 which resides within the flat band, E1 connecting LL1 with LL2, and E2 linking LL2 with higher-lying LL3. The right side of Fig. 5(c) shows the localization of the wave
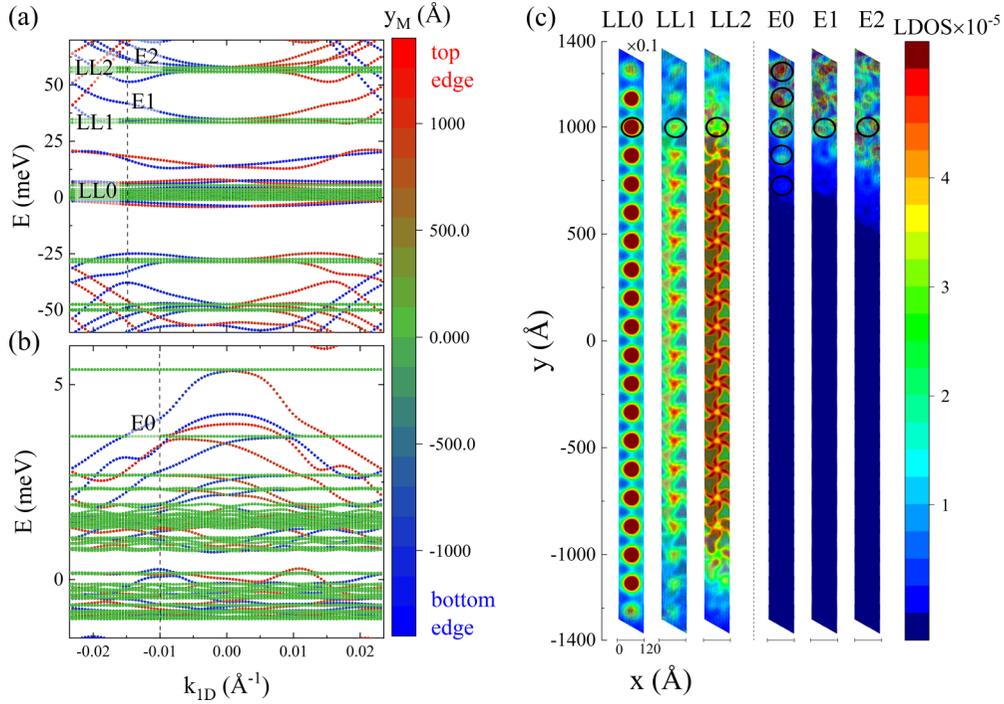
FIG. 5. Electronic structure and wave functions of the hBN-MATBG ribbon in the magnetic field. (a) Band structure of the 20 moiré unit cells wide hBN-MATBG nanoribbon in perpendicular magnetic field $B_z = 4$ T without Zeeman splitting. Both LLs (LL0, LL1, LL2) and edge states (E1, E2) are shown. The color scale denotes the wave-function localization, with top (bottom) edge states marked by red (blue) dots. Green dots mark bulk states predominantly localized in the center of the sample. (b) Zoom-in into the flat band, revealing its substructure in the magnetic field, again with the moiré edge states (E0) crossing between the moiré LLs. (c) LDOS for the bulk and edge states, which are marked in (a) and (b). The specific values of k_{1D} for which they were calculated are indicated with a black dashed line. The left side of (c) shows selected bulk states: the flat band (LL0), the first LL (LL1), and the second LL (LL2). On the right, the edge states are shown: E0, which is localized within the flat band; E1 which connects LL1 and LL2; and E2, which connects LL2 with LL3 (the third LL). The black circles correspond to the moiré centers, which are fixed around the AA-stacked atoms in the unit cell. Note that the color scale for LL0 is scaled by 0.1 compared to the rest of the LDOS plots in (c).

function for these three cases and, in particular, what its relation is to the moiré centers marked with black circles. E0 is predominantly localized within the moiré centers close to the edge of the sample, and the trivial edge states in the energy gap between LL0 and LL1 around $E = 25$ meV behave in a similar manner. In the case of E1, the AA-stacking localization can still be spotted, although the effect is less prominent. As for E2, there is no correspondence between the wave function localization and the moiré center's position. This is to be expected, since this state is separated by over 50 meV from the flat band, and moiré potential does not play a role here.

D. Evolution of the microscopic wave function's properties

We now turn to the analysis of how the LDOS changes in response to the magnetic field. For concreteness, we define a moiré center as the region within the dashed circle marked in Fig. 6(a). This figure shows that there are strong differences between LL0, LL1, LL2, and those three states should be easily distinguished in scanning tunneling spectroscopy type experiments. We investigate how much of the wave function is localized within the moiré center and how this distribution evolves with an increasing magnetic field. The outcomes of this calculation are presented in Fig. 6(b), where we

quantitatively compare the wave function localization for LL0, LL1, and LL2. We also show that, in the flat-band case, as the magnetic field increases, the wave function flows out of the moiré center and distributes more evenly over the sample, as the effect of the magnetic field becomes dominant over the effect of the moiré potential. Therefore, one can observe the decreasing character of the red line in Fig. 6(b). In the case of LL1 and LL2, denoted by green and blue lines, respectively, there is a similar trend present, however, it cannot be observed for a larger range of B_z, since with the increase of the magnetic field these LLs are not unequivocally defined.

We have also focused on the moiré center nearest to the edge of the sample, as depicted in Fig. 6(c). Here, we investigate how much of the wave function localizes in the immediate vicinity of this center as a function of the wave vector k_{1D}. These findings are summarized in Fig. 6(d), where a clear distinction between E0, E1, and E2 is shown. This observation reinforces our classification of the three types of edge states. The evolution of these edge states as a function of k_{1D} looks nontrivial and warrants a more extensive study in the future. Their behavior as a function of k_{1D} is characterized by qualitative differences, with E0 exhibiting a local minimum, E1 decaying exponentially, while E2 remaining mostly flat. These features could potentially be verified by experiments.
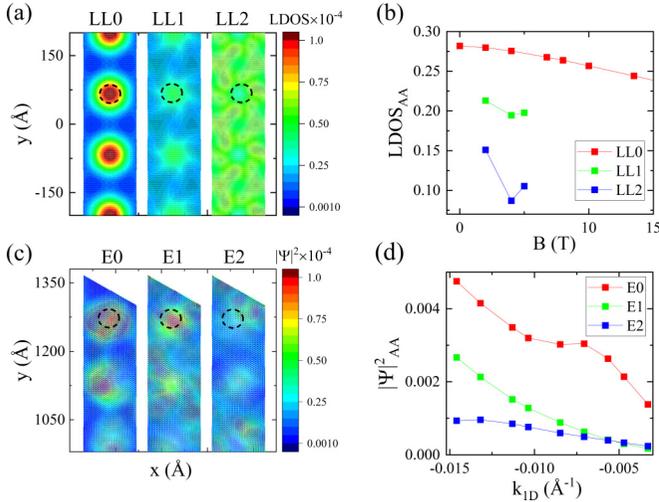
FIG. 6. LDOS within moiré AA centers for bulk and edge states in a magnetic field for an hBN-MATBG ribbon. (a) Real-space distribution of LDOS for selected bulk LLs (LL0-LL2) shown around the center of the sample for $B_z = 4$ T. (b) Corresponding integrated LDOS calculated for the moiré center defined as the region within a black circle centered around AA stacked atoms with the radius $r = 25$ Å. (c) Wave-function density $|\Psi|^2$ plot of selected edge states, from left: E0, which lies within the flat band, E1 connecting LL1 and LL2, and E2, linking LL2 with LL3. (d) Similar to (b), $|\Psi|^2$ analysis, with integrated density calculated for the moiré center closest to the edge of the ribbon.

V. CONCLUSIONS

In this paper, we analyzed the microscopic properties of MATBG on top of hBN under the influence of a magnetic field. We have studied systems consisting of up to 1 000 000 atoms (85 moiré unit cells) and have established that for a ribbon's width larger than 20 unit cells, hybridization between the wave functions of the edge states is negligible. For such wide ribbons, we studied the Hofstadter spectrum and determined the in-gap Chern numbers from the number of chiral edge states crossing the energy gaps. At low magnetic field, a corresponding Wannier diagram has been obtained and used to identify noninteracting, insulating states, finding qualitative agreement with the experiments. We have analyzed a competition between the moiré localization potential and the effect of a magnetic field. The microscopic properties of the wave functions were determined and three types of bulk and edge states were identified, namely, moiré, mixed, and conventional states. We have examined their evolution as a function of the magnetic field and the wave vector. While our analysis was primarily restricted to single-particle physics without electrostatic corrections for doping away from $\nu = 0$, we anticipate that our findings can provide valuable guidance for future scanning tunneling microscopy measurements and help to experimentally establish properties of microscopic wave functions in TBG.

ACKNOWLEDGMENTS

APPENDIX A: MOIRÉ FLAT-BAND BREAKDOWN

A recent experiment [194] has shown that the characteristic flat-band LDOS localization around the moiré centers of the superlattice remains intact even close to the edge, as long as the sample contains a complete moiré spot. However, if the edge of the sample cuts through the AA region, the flat-band LDOS will no longer be localized in that area. Our model correctly captures these features. In Fig. 7, we present three different ways of terminating our nanoribbon. In the first case, we preserve the whole moiré center at the edge ($\vec{S} = 0$), while in the second and third, we shift our original unit cell by a vector $\vec{S} = -1/3\vec{L}$ and $\vec{S} = -1/2\vec{L}$, respectively [$\vec{L} = \vec{L}_1 + \vec{L}_2$, see Eqs. (1)]. One can notice that in the first case, there is a complete moiré center localized close to the edge, but for the other two choices of the edge, the LDOS fades away in that region. We have compared our results with the experimental data extracted from Ref. [194] in Fig. 8. Both in the experimental result and our spatially integrated LDOS result, there is a clear change in the electron density when the edge cuts through the AA moiré region. This confirms that our model is capable of capturing local physics near the edges of MATBG system under study.
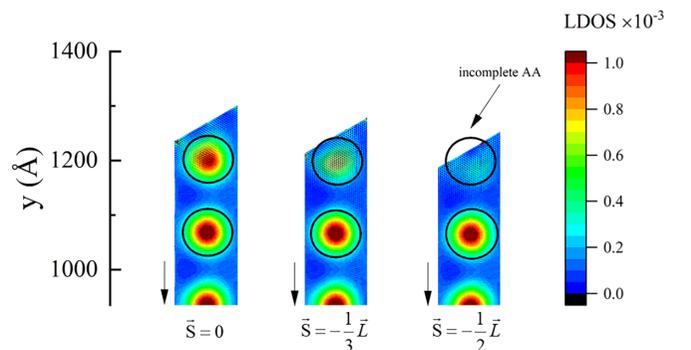
FIG. 7. LDOS near the top edge of 20 moiré unit cell ribbons for different choices of boundary termination. Different cuts are parametrized by the shift vector S. Black circles denote the AA regions.
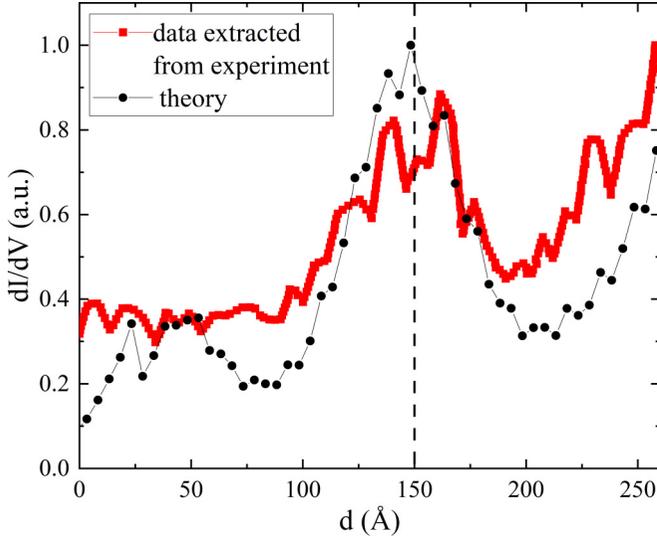
FIG. 8. Comparison of dI/dV spectrum near the edge of the MATBG sample extracted from Ref. [194] with our spatially integrated LDOS calculation shows the effect of flat-band breakdown. Distance d is measured from the edge of the sample. The dashed line indicates the center of one of the AA regions.

APPENDIX B: EFFECT OF HBN SUBSTRATE ON HOFSTADTER SPECTRUM AND WANNIER DIAGRAMS

Now we elaborate further on the role of an hBN substrate. As outlined in Sec. II, we consider the presence of hBN on only one side of the sample and model its influence by introducing a staggered potential. It is important to emphasize that

if one were to add a microscopically realistic layer of hBN, there would be a number of additional effects. The inherent lattice mismatch between hBN and graphene typically gives rise to an extra moiré pattern with a period comparable to that of MATBG, which could potentially affect the flat bands. One of the current experimental approaches is to twist the hBN layer with respect to MATBG by a small angle to match their moiré patterns to maximally flatten the bands. Consequently, our treatment of hBN should be treated as a simplified one. In our approach, we take the staggered potential to be 10 meV, consistent with *ab initio* calculations [188,189]. To gain a clearer understanding of its impact, we here isolate the influence of hBN on the Hofstadter spectrum. In Figs. 9(a) and 9(d), we reproduce the bulk states' band structure in $B_z = 0\,\mathrm{T}$, aiding in identifying the sources of high densities of states in the Hofstadter spectrum for $B_z \approx 0\,\mathrm{T}$. Comparison of the fractal spectra in a large energy window shows a similar trend, demonstrating the same features for a sample Fig. 9(b) without and Fig. 9(c) with the hBN substrate. However, a closer examination of the zoomed-in spectrum in Figs. 9(e)–9(f) reveals significant differences between Figs. 9(e) MATBG and 9(f) hBN-MATBG. First, there is a trivial gap with no edge states crossing through it, which emerges around the zero energy for magnetic fields between 0–5 T. The spectrum displays numerous additional gaps in general, resulting in a much richer substructure of the flat band compared to pristine MATBG. These gaps are generally narrower and remain open within limited ranges of the magnetic field values.

The effects associated with the influence of hBN on MATBG become even more evident when examining the Wannier diagrams. Figures 10(a) and 10(b) pertain to a
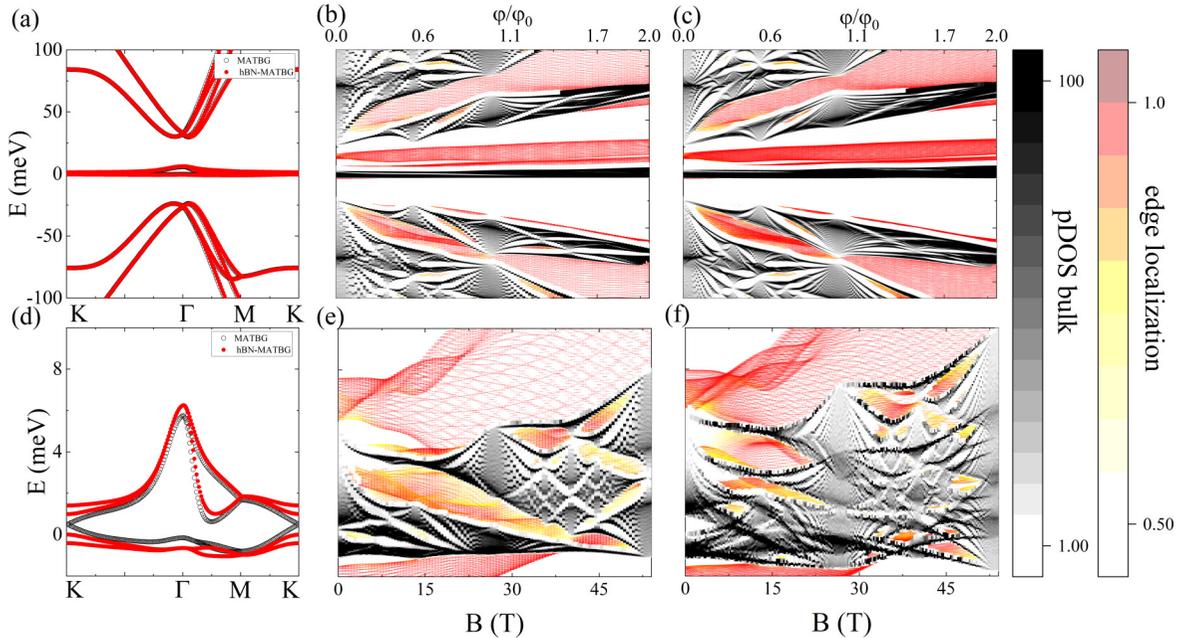
FIG. 9. The influence of the hBN substrate on the band structure and the Hofstadter spectrum. (a) Flat and remote bands around the Fermi level. The black circles represent a pure MATBG sample, while the red dots depict the impact of the hBN substrate. The Hofstadter spectrum (b) without and (c) with the hBN substrate effect. (d)–(f) Zoom-in to the flat band. (e) and (f) provide a corresponding close-up view of the MATBG fractal spectrum without and with the effect of hBN, respectively.
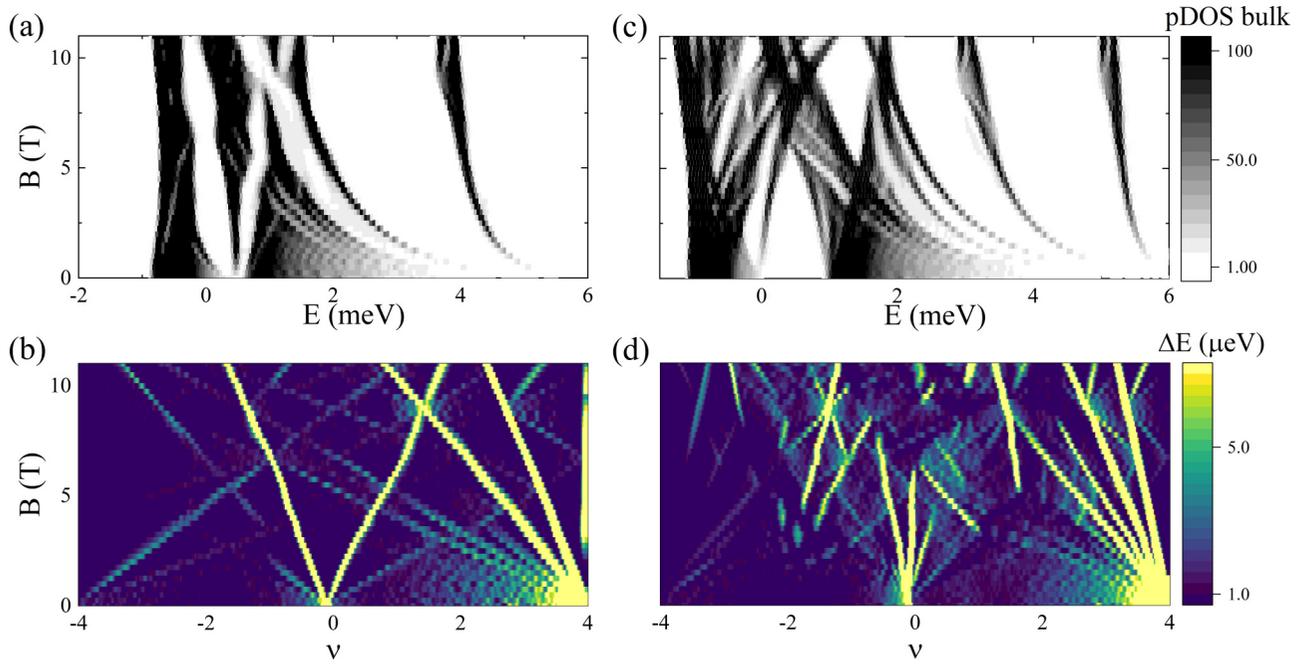
FIG. 10. The role of an hBN substrate on the Wannier diagram in the flat band of MATBG. (a) Hofstadter spectrum illustrating the bulk states of the flat band in MATBG without the hBN substrate. (b) Corresponding Wannier diagram for the spectrum shown in (a). Characteristic V-shape picture around $\nu = 0$ as seen in the experiments [16,123]. (c) Fractal spectrum, similar to (a), but accounting for the effect of hBN. (d) Wannier diagram corresponding to (c), using the same color scale as (b).

pristine MATBG sample, while Figs. 10(c) and 10(d) correspond to MATBG on hBN. Once again, it is apparent that the presence of hBN induces the emergence of numerous additional band gaps, particularly for larger magnetic

fields. The Wannier diagram depicted in Fig. 10(b) can be compared to the compressibility measurements for unaligned devices [16,123], wherein a similar V-shape stemming from the charge neutrality point can be observed.

[1] Y. Cao, V. Fatemi, A. Demir, S. Fang, S. L. Tomarken, J. Y. Luo, J. D. Sanchez-Yamagishi, K. Watanabe, T. Taniguchi, E. Kaxiras, R. C. Ashoori, and P. Jarillo-Herrero, Correlated insulator behaviour at half-filling in magic-angle graphene superlattices, Nature (London) **556**, 80 (2018).

[2] Y. Cao, V. Fatemi, S. Fang, K. Watanabe, T. Taniguchi, E. Kaxiras, and P. Jarillo-Herrero, Unconventional superconductivity in magic-angle graphene superlattices, Nature (London) **556**, 43 (2018).

[3] M. Yankowitz, S. Chen, H. Polshyn, Y. Zhang, K. Watanabe, T. Taniguchi, D. Graf, A. F. Young, and C. R. Dean, Tuning superconductivity in twisted bilayer graphene, Science **363**, 1059 (2019).

[4] A. L. Sharpe, E. J. Fox, A. W. Barnard, J. Finney, K. Watanabe, T. Taniguchi, M. A. Kastner, and D. Goldhaber-Gordon, Emergent ferromagnetism near three-quarters filling in twisted bilayer graphene, Science **365**, 605 (2019).

[5] Y. Xie, B. Lian, B. Jäck, X. Liu, C.-L. Chiu, K. Watanabe, T. Taniguchi, B. A. Bernevig, and A. Yazdani, Spectroscopic signatures of many-body correlations in magic-angle twisted bilayer graphene, Nature (London) **572**, 101 (2019).

[6] Y. Cao, D. Rodan-Legrain, J. M. Park, N. F. Q. Yuan, K. Watanabe, T. Taniguchi, R. M. Fernandes, L. Fu, and P. Jarillo-Herrero, Nematicity and competing orders in superconducting magic-angle graphene, Science **372**, 264 (2021).

[7] K. Kim, A. DaSilva, S. Huang, B. Fallahazad, S. Larentis, T. Taniguchi, K. Watanabe, B. J. LeRoy, A. H. MacDonald, and E. Tutuc, Tunable moiré bands and strong correlations in small-twist-angle bilayer graphene, Proc. Natl. Acad. Sci. USA **114**, 3364 (2017).

[8] X. Lu, P. Stepanov, W. Yang, M. Xie, M. A. Aamir, I. Das, C. Urgell, K. Watanabe, T. Taniguchi, G. Zhang, A. Bachtold, A. H. MacDonald, and D. K. Efetov, Superconductors, orbital magnets and correlated states in magic-angle bilayer graphene, Nature (London) **574**, 653 (2019).

[9] A. Uri, S. Grover, Y. Cao, J. A. Crosse, K. Bagani, D. Rodan-Legrain, Y. Myasoedov, K. Watanabe, T. Taniguchi, P. Moon, M. Koshino, P. Jarillo-Herrero, and E. Zeldov, Mapping the twist-angle disorder and Landau levels in magic-angle graphene, Nature (London) **581**, 47 (2020).

[10] L. Balents, C. R. Dean, D. K. Efetov, and A. F. Young, Superconductivity and strong correlations in moiré flat bands, Nat. Phys. **16**, 725 (2020).

[11] D. Wong, K. P. Nuckolls, M. Oh, B. Lian, Y. Xie, S. Jeon, K. Watanabe, T. Taniguchi, B. A. Bernevig, and A. Yazdani, Cascade of electronic transitions in magic-angle twisted bilayer graphene, Nature (London) **582**, 198 (2020).

[12] U. Zondiner, A. Rozen, D. Rodan-Legrain, Y. Cao, R. Queiroz, T. Taniguchi, K. Watanabe, Y. Oreg, F. von Oppen, A. Stern, E. Berg, P. Jarillo-Herrero, and S. Ilani, Cascade of phase

transitions and Dirac revivals in magic-angle graphene, Nature (London) **582**, 203 (2020).

[13] M. Serlin, C. L. Tschirhart, H. Polshyn, Y. Zhang, J. Zhu, K. Watanabe, T. Taniguchi, L. Balents, and A. F. Young, Intrinsic quantized anomalous Hall effect in a moiré heterostructure, Science **367**, 900 (2020).

[14] P. Stepanov, I. Das, X. Lu, A. Fahimniya, K. Watanabe, T. Taniguchi, F. H. L. Koppens, J. Lischner, L. Levitov, and D. K. Efetov, Untying the insulating and superconducting orders in magic-angle graphene, Nature (London) **583**, 375 (2020).

[15] S. Wu, Z. Zhang, K. Watanabe, T. Taniguchi, and E. Y. Andrei, Chern insulators, van Hove singularities and topological flat bands in magic-angle twisted bilayer graphene, Nat. Mater. **20**, 488 (2021).

[16] I. Das, X. Lu, J. Herzog-Arbeitman, Z.-D. Song, K. Watanabe, T. Taniguchi, B. A. Bernevig, and D. K. Efetov, Symmetry-broken Chern insulators and Rashba-like Landau-level crossings in magic-angle bilayer graphene, Nat. Phys. **17**, 710 (2021).

[17] P. Stepanov, M. Xie, T. Taniguchi, K. Watanabe, X. Lu, A. H. MacDonald, B. A. Bernevig, and D. K. Efetov, Competing zero-field Chern insulators in superconducting twisted bilayer graphene, Phys. Rev. Lett. **127**, 197701 (2021).

[18] A. Rozen, J. M. Park, U. Zondiner, Y. Cao, D. Rodan-Legrain, T. Taniguchi, K. Watanabe, Y. Oreg, A. Stern, E. Berg, P. Jarillo-Herrero, and S. Ilani, Entropic evidence for a Pomeranchuk effect in magic-angle graphene, Nature (London) **592**, 214 (2021).

[19] Y. Saito, J. Ge, K. Watanabe, T. Taniguchi, and A. F. Young, Independent superconductors and correlated insulators in twisted bilayer graphene, Nat. Phys. **16**, 926 (2020).

[20] R. Bistritzer and A. H. MacDonald, Moiré bands in twisted double-layer graphene, Proc. Natl. Acad. Sci. USA **108**, 12233 (2011).

[21] J. M. B. Lopes dos Santos, N. M. R. Peres, and A. H. Castro Neto, Graphene bilayer with a twist: Electronic structure, Phys. Rev. Lett. **99**, 256802 (2007).

[22] B. A. Bernevig, Z.-D. Song, N. Regnault, and B. Lian, Twisted bilayer graphene. I. Matrix elements, approximations, perturbation theory, and a $k \cdot p$ two-band model, Phys. Rev. B **103**, 205411 (2021).

[23] Z.-D. Song, B. Lian, N. Regnault, and B. A. Bernevig, Twisted bilayer graphene. II. Stable symmetry anomaly, Phys. Rev. B **103**, 205412 (2021).

[24] B. A. Bernevig, Z.-D. Song, N. Regnault, and B. Lian, Twisted bilayer graphene. III. interacting Hamiltonian and exact symmetries, Phys. Rev. B **103**, 205413 (2021).

[25] B. Lian, Z.-D. Song, N. Regnault, D. K. Efetov, A. Yazdani, and B. A. Bernevig, Twisted bilayer graphene. IV. Exact insulator ground states and phase diagram, Phys. Rev. B **103**, 205414 (2021).

[26] B. A. Bernevig, B. Lian, A. Cowsik, F. Xie, N. Regnault, and Z.-D. Song, Twisted bilayer graphene. V. Exact analytic many-body excitations in Coulomb Hamiltonians: Charge gap, goldstone modes, and absence of cooper pairing, Phys. Rev. B **103**, 205415 (2021).

[27] J. Kang and O. Vafek, Non-Abelian Dirac node braiding and near-degeneracy of correlated phases at odd integer filling

in magic-angle twisted bilayer graphene, Phys. Rev. B **102**, 035161 (2020).

[28] J. Jung, A. Raoux, Z. Qiao, and A. H. MacDonald, *Ab initio* theory of moiré superlattice bands in layered two-dimensional materials, Phys. Rev. B **89**, 205414 (2014).

[29] H. C. Po, L. Zou, A. Vishwanath, and T. Senthil, Origin of Mott insulating behavior and superconductivity in twisted bilayer graphene, Phys. Rev. X **8**, 031089 (2018).

[30] N. F. Q. Yuan and L. Fu, Model for the metal-insulator transition in graphene superlattices and beyond, Phys. Rev. B **98**, 045103 (2018).

[31] H. Guo, X. Zhu, S. Feng, and R. T. Scalettar, Pairing symmetry of interacting fermions on a twisted bilayer graphene superlattice, Phys. Rev. B **97**, 235453 (2018).

[32] M. Xie and A. H. MacDonald, Weak-field Hall resistivity and spin-valley flavor symmetry breaking in magic-angle twisted bilayer graphene, Phys. Rev. Lett. **127**, 196401 (2021).

[33] F. Xie, A. Cowsik, Z.-D. Song, B. Lian, B. A. Bernevig, and N. Regnault, Twisted bilayer graphene. VI. An exact diagonalization study at nonzero integer filling, Phys. Rev. B **103**, 205416 (2021).

[34] P. Potasz, M. Xie, and A. H. MacDonald, Exact diagonalization for magic-angle twisted bilayer graphene, Phys. Rev. Lett. **127**, 147203 (2021).

[35] J. F. Dodaro, S. A. Kivelson, Y. Schattner, X. Q. Sun, and C. Wang, Phases of a phenomenological model of twisted bilayer graphene, Phys. Rev. B **98**, 075154 (2018).

[36] C.-C. Liu, L.-D. Zhang, W.-Q. Chen, and F. Yang, Chiral spin density wave and $d + id$ superconductivity in the magic-angle-twisted bilayer graphene, Phys. Rev. Lett. **121**, 217001 (2018).

[37] X. Y. Xu, K. T. Law, and P. A. Lee, Kekulé valence bond order in an extended Hubbard model on the honeycomb lattice with possible applications to twisted bilayer graphene, Phys. Rev. B **98**, 121406(R) (2018).

[38] L. Rademaker and P. Mellado, Charge-transfer insulation in twisted bilayer graphene, Phys. Rev. B **98**, 235158 (2018).

[39] M. Koshino, N. F. Q. Yuan, T. Koretsune, M. Ochi, K. Kuroki, and L. Fu, Maximally localized Wannier orbitals and the extended Hubbard model for twisted bilayer graphene, Phys. Rev. X **8**, 031087 (2018).

[40] A. Thomson, S. Chatterjee, S. Sachdev, and M. S. Scheurer, Triangular antiferromagnetism on the honeycomb lattice of twisted bilayer graphene, Phys. Rev. B **98**, 075109 (2018).

[41] F. Guinea and N. R. Walet, Electrostatic effects, band distortions, and superconductivity in twisted graphene bilayers, Proc. Natl. Acad. Sci. USA **115**, 13174 (2018).

[42] M. Ochi, M. Koshino, and K. Kuroki, Possible correlated insulating states in magic-angle twisted bilayer graphene under strongly competing interactions, Phys. Rev. B **98**, 081102(R) (2018).

[43] H. Isobe, N. F. Q. Yuan, and L. Fu, Unconventional superconductivity and density waves in twisted bilayer graphene, Phys. Rev. X **8**, 041041 (2018).

[44] C. Xu and L. Balents, Topological superconductivity in twisted multilayer graphene, Phys. Rev. Lett. **121**, 087001 (2018).

[45] F. Wu, A. H. MacDonald, and I. Martin, Theory of phonon-mediated superconductivity in twisted bilayer graphene, Phys. Rev. Lett. **121**, 257001 (2018).

[46] T. J. Peltonen, R. Ojajärvi, and T. T. Heikkilä, Mean-field theory for superconductivity in twisted bilayer graphene, Phys. Rev. B **98**, 220504(R) (2018).

[47] M. Fidrysiak, M. Zegrodnik, and J. Spałek, Unconventional topological superconductivity and phase diagram for an effective two-orbital model as applied to twisted bilayer graphene, Phys. Rev. B **98**, 085436 (2018).

[48] J. M. Pizarro, M. J. Calderón, and E. Bascones, The nature of correlations in the insulating states of twisted bilayer graphene, J. Phys. Commun. **3**, 035024 (2019).

[49] J. Kang and O. Vafek, Strong coupling phases of partially filled twisted bilayer graphene narrow bands, Phys. Rev. Lett. **122**, 246401 (2019).

[50] J. Liu, J. Liu, and X. Dai, Pseudo Landau level representation of twisted bilayer graphene: Band topology and implications on the correlated insulating phase, Phys. Rev. B **99**, 155415 (2019).

[51] B. Roy and V. Juričić, Unconventional superconductivity in nearly flat bands in twisted bilayer graphene, Phys. Rev. B **99**, 121407(R) (2019).

[52] S. Ray, J. Jung, and T. Das, Wannier pairs in superconducting twisted bilayer graphene and related systems, Phys. Rev. B **99**, 134515 (2019).

[53] Y.-Z. You and A. Vishwanath, Superconductivity from valley fluctuations and approximate SO(4) symmetry in a weak coupling theory of twisted bilayer graphene, npj Quantum Mater. **4**, 16 (2019).

[54] G. Tarnopolsky, A. J. Kruchkov, and A. Vishwanath, Origin of magic angles in twisted bilayer graphene, Phys. Rev. Lett. **122**, 106405 (2019).

[55] Y.-H. Zhang, D. Mao, Y. Cao, P. Jarillo-Herrero, and T. Senthil, Nearly flat Chern bands in moiré superlattices, Phys. Rev. B **99**, 075127 (2019).

[56] J. M. Pizarro, M. Rösner, R. Thomale, R. Valentí, and T. O. Wehling, Internal screening and dielectric engineering in magic-angle twisted bilayer graphene, Phys. Rev. B **100**, 161102(R) (2019).

[57] Y. Da Liao, Z. Y. Meng, and X. Y. Xu, Valence bond orders at charge neutrality in a possible two-orbital extended Hubbard model for twisted bilayer graphene, Phys. Rev. Lett. **123**, 157601 (2019).

[58] Z. Song, Z. Wang, W. Shi, G. Li, C. Fang, and B. A. Bernevig, All magic angles in twisted bilayer graphene are topological, Phys. Rev. Lett. **123**, 036401 (2019).

[59] J. Liu, Z. Ma, J. Gao, and X. Dai, Quantum valley Hall effect, orbital magnetism, and anomalous Hall effect in twisted multilayer graphene systems, Phys. Rev. X **9**, 031021 (2019).

[60] N. Bultinck, E. Khalaf, S. Liu, S. Chatterjee, A. Vishwanath, and M. P. Zaletel, Ground state and hidden symmetry of magic-angle graphene at even integer filling, Phys. Rev. X **10**, 031034 (2020).

[61] Y. Zhang, Z. Hou, Y.-X. Zhao, Z.-H. Guo, Y.-W. Liu, S.-Y. Li, Y.-N. Ren, Q.-F. Sun, and L. He, Correlation-induced valley splitting and orbital magnetism in a strain-induced zero-energy flatband in twisted bilayer graphene near the magic angle, Phys. Rev. B **102**, 081403(R) (2020).

[62] M. Xie and A. H. MacDonald, Nature of the correlated insulator states in twisted bilayer graphene, Phys. Rev. Lett. **124**, 097601 (2020).

[63] O. Vafek and J. Kang, Renormalization group study of hidden symmetry in twisted bilayer graphene with Coulomb interactions, Phys. Rev. Lett. **125**, 257602 (2020).

[64] C. Repellin, Z. Dong, Y.-H. Zhang, and T. Senthil, Ferromagnetism in narrow bands of moiré superlattices, Phys. Rev. Lett. **124**, 187601 (2020).

[65] T. Soejima, D. E. Parker, N. Bultinck, J. Hauschild, and M. P. Zaletel, Efficient simulation of moiré materials using the density matrix renormalization group, Phys. Rev. B **102**, 205111 (2020).

[66] D. E. Parker, T. Soejima, J. Hauschild, M. P. Zaletel, and N. Bultinck, Strain-induced quantum phase transitions in magic-angle graphene, Phys. Rev. Lett. **127**, 027601 (2021).

[67] A. Kumar, M. Xie, and A. H. MacDonald, Lattice collective modes from a continuum model of magic-angle twisted bilayer graphene, Phys. Rev. B **104**, 035119 (2021).

[68] P. J. Ledwith, E. Khalaf, and A. Vishwanath, Strong coupling theory of magic-angle graphene: A pedagogical introduction, Ann. Phys. **435**, 168646 (2021).

[69] Y. H. Kwan, G. Wagner, T. Soejima, M. P. Zaletel, S. H. Simon, S. A. Parameswaran, and N. Bultinck, Kekulé spiral order at all nonzero integer fillings in twisted bilayer graphene, Phys. Rev. X **11**, 041063 (2021).

[70] J. Vahedi, R. Peters, A. Missaoui, A. Honecker, and G. T. de Laissardiere, Magnetism of magic-angle twisted bilayer graphene, SciPost Phys. **11**, 083 (2021).

[71] C. Lewandowski, S. Nadj-Perge, and D. Chowdhury, Does filling-dependent band renormalization aid pairing in twisted bilayer graphene? npj Quantum Mater. **6**, 82 (2021).

[72] B.-B. Chen, Y. D. Liao, Z. Chen, O. Vafek, J. Kang, W. Li, and Z. Y. Meng, Realization of topological Mott insulator in a twisted bilayer graphene lattice model, Nat. Commun. **12**, 5480 (2021).

[73] S. Chatterjee, M. Ippoliti, and M. P. Zaletel, Skyrmion superconductivity: DMRG evidence for a topological route to superconductivity, Phys. Rev. B **106**, 035421 (2022).

[74] X. Liu, R. Peng, Z. Sun, and J. Liu, Moiré phonons in magic-angle twisted bilayer graphene, Nano Lett. **22**, 7791 (2022).

[75] M. Romanova and V. Vlček, Stochastic many-body calculations of moiré states in twisted bilayer graphene at high pressures, npj Comput. Mater. **8**, 11 (2022).

[76] S. Zhang, X. Lu, and J. Liu, Correlated insulators, density wave states, and their nonlinear optical response in magic-angle twisted bilayer graphene, Phys. Rev. Lett. **128**, 247402 (2022).

[77] D. V. Chichinadze, L. Classen, Y. Wang, and A. V. Chubukov, SU(4) symmetry in twisted bilayer graphene: An itinerant perspective, Phys. Rev. Lett. **128**, 227601 (2022).

[78] H. Ochoa and R. M. Fernandes, Degradation of phonons in disordered moiré superlattices, Phys. Rev. Lett. **128**, 065901 (2022).

[79] Y. H. Kwan, G. Wagner, N. Bultinck, S. H. Simon, and S. A. Parameswaran, Skyrmions in twisted bilayer graphene: Stability, pairing, and crystallization, Phys. Rev. X **12**, 031020 (2022).

[80] J. S. Hofmann, E. Khalaf, A. Vishwanath, E. Berg, and J. Y. Lee, Fermionic Monte Carlo study of a realistic model of twisted bilayer graphene, Phys. Rev. X **12**, 011061 (2022).

[81] Z.-D. Song and B. A. Bernevig, Magic-angle twisted bilayer graphene as a topological heavy fermion problem, Phys. Rev. Lett. **129**, 047601 (2022).

[82] F. Schindler, O. Vafek, and B. A. Bernevig, Trions in twisted bilayer graphene, Phys. Rev. B **105**, 155135 (2022).

[83] Z. Han and S. A. Kivelson, Pair density wave and reentrant superconducting tendencies originating from valley polarization, Phys. Rev. B **105**, L100509 (2022).

[84] D. Călugăru, N. Regnault, M. Oh, K. P. Nuckolls, D. Wong, R. L. Lee, A. Yazdani, O. Vafek, and B. A. Bernevig, Spectroscopy of twisted bilayer graphene correlated insulators, Phys. Rev. Lett. **129**, 117602 (2022).

[85] J. P. Hong, T. Soejima, and M. P. Zaletel, Detecting symmetry breaking in magic angle graphene using scanning tunneling microscopy, Phys. Rev. Lett. **129**, 147001 (2022).

[86] C. N. Breiø and B. M. Andersen, Chern insulator phases and spontaneous spin and valley order in a moiré lattice model for magic-angle twisted bilayer graphene, Phys. Rev. B **107**, 165114 (2023).

[87] Y. Mao, D. Guerci, and C. Mora, Supermoiré low-energy effective theory of twisted trilayer graphene, Phys. Rev. B **107**, 125423 (2023).

[88] F. Xie, J. Kang, B. A. Bernevig, O. Vafek, and N. Regnault, Phase diagram of twisted bilayer graphene at filling factor $\nu = \pm 3$, Phys. Rev. B **107**, 075156 (2023).

[89] E. Morissette, J.-X. Lin, D. Sun, L. Zhang, S. Liu, D. Rhodes, K. Watanabe, T. Taniguchi, J. Hone, J. Pollanen, M. S. Scheurer, M. Lilly, A. Mounce, and J. I. A. Li, Dirac revivals drive a resonance response in twisted bilayer graphene, Nat. Phys. **19**, 1156 (2023).

[90] G. Pan, X. Zhang, H. Lu, H. Li, B.-B. Chen, K. Sun, and Z. Y. Meng, Thermodynamic characteristic for a correlated flat-band system with a quantum anomalous Hall ground state, Phys. Rev. Lett. **130**, 016401 (2023).

[91] I. Mandal and R. M. Fernandes, Valley-polarized nematic order in twisted moiré systems: In-plane orbital magnetism and crossover from non-Fermi liquid to Fermi liquid, Phys. Rev. B **107**, 125142 (2023).

[92] S. K. Firoz Islam, A. Y. Zyuzin, and A. A. Zyuzin, Unconventional superconductivity with preformed pairs in twisted bilayer graphene, Phys. Rev. B **107**, L060503 (2023).

[93] E. Suárez Morell, J. D. Correa, P. Vargas, M. Pacheco, and Z. Barticevic, Flat bands in slightly twisted bilayer graphene: Tight-binding calculations, Phys. Rev. B **82**, 121407(R) (2010).

[94] J. Kang and O. Vafek, Symmetry, maximally localized Wannier states, and a low-energy model for twisted bilayer graphene narrow bands, Phys. Rev. X **8**, 031088 (2018).

[95] B. Padhi, C. Setty, and P. W. Phillips, Doped twisted bilayer graphene near magic angles: Proximity to Wigner crystallization, not Mott insulation, Nano Lett. **18**, 6175 (2018).

[96] X. Hu, T. Hyart, D. I. Pikulin, and E. Rossi, Geometric and conventional contribution to the superfluid weight in twisted bilayer graphene, Phys. Rev. Lett. **123**, 237002 (2019).

[97] J. H. Wilson, Y. Fu, S. Das Sarma, and J. H. Pixley, Disorder in twisted bilayer graphene, Phys. Rev. Res. **2**, 023325 (2020).

[98] F. Xie, Z. Song, B. Lian, and B. A. Bernevig, Topology-bounded superfluid weight in twisted bilayer graphene, Phys. Rev. Lett. **124**, 167002 (2020).

[99] K. Hejazi, X. Chen, and L. Balents, Hybrid Wannier Chern bands in magic angle twisted bilayer graphene and the quantized anomalous Hall effect, Phys. Rev. Res. **3**, 013242 (2021).

[100] B. Padhi, A. Tiwari, T. Neupert, and S. Ryu, Transport across twist angle domains in moiré graphene, Phys. Rev. Res. **2**, 033458 (2020).

[101] N. Bultinck, S. Chatterjee, and M. P. Zaletel, Mechanism for anomalous Hall ferromagnetism in twisted bilayer graphene, Phys. Rev. Lett. **124**, 166601 (2020).

[102] S. Chatterjee, N. Bultinck, and M. P. Zaletel, Symmetry breaking and skyrmionic transport in twisted bilayer graphene, Phys. Rev. B **101**, 165141 (2020).

[103] A. Julku, T. J. Peltonen, L. Liang, T. T. Heikkilä, and P. Törmä, Superfluid weight and Berezinskii-Kosterlitz-Thouless transition temperature of twisted bilayer graphene, Phys. Rev. B **101**, 060505(R) (2020).

[104] Y. H. Kwan, G. Wagner, N. Chakraborty, S. H. Simon, and S. A. Parameswaran, Domain wall competition in the Chern insulating regime of twisted bilayer graphene, Phys. Rev. B **104**, 115404 (2021).

[105] S. Liu, E. Khalaf, J. Y. Lee, and A. Vishwanath, Nematic topological semimetal and insulator in magic-angle bilayer graphene at charge neutrality, Phys. Rev. Res. **3**, 013033 (2021).

[106] E. Khalaf, S. Chatterjee, N. Bultinck, M. P. Zaletel, and A. Vishwanath, Charged skyrmions and topological origin of superconductivity in magic-angle graphene, Sci. Adv. **7**, eabf5299 (2021).

[107] V. Peri, Z.-D. Song, B. A. Bernevig, and S. D. Huber, Fragile topology and flat-band superconductivity in the strong-coupling regime, Phys. Rev. Lett. **126**, 027002 (2021).

[108] C. Huang, X. Zhang, G. Pan, H. Li, K. Sun, X. Dai, and Z. Y. Meng, Evolution from quantum anomalous Hall insulator to heavy-fermion semimetal in twisted bilayer graphene, arXiv:2304.14064.

[109] F. M. Faulstich, K. D. Stubbs, Q. Zhu, T. Soejima, R. Dilip, H. Zhai, R. Kim, M. P. Zaletel, Garnet Kin-Lic Chan, and L. Lin, Interacting models for twisted bilayer graphene: A quantum chemistry approach, Phys. Rev. B **107**, 235123 (2023).

[110] S. L. Tomarken, Y. Cao, A. Demir, K. Watanabe, T. Taniguchi, P. Jarillo-Herrero, and R. C. Ashoori, Electronic compressibility of magic-angle graphene superlattices, Phys. Rev. Lett. **123**, 046601 (2019).

[111] K. P. Nuckolls, M. Oh, D. Wong, B. Lian, K. Watanabe, T. Taniguchi, B. A. Bernevig, and A. Yazdani, Strongly correlated Chern insulators in magic-angle twisted bilayer graphene, Nature (London) **588**, 610 (2020).

[112] H. S. Arora, R. Polski, Y. Zhang, A. Thomson, Y. Choi, H. Kim, Z. Lin, I. Z. Wilson, X. Xu, J.-H. Chu, K. Watanabe, T. Taniguchi, J. Alicea, and S. Nadj-Perge, Superconductivity in metallic twisted bilayer graphene stabilized by WSe$_2$, Nature (London) **583**, 379 (2020).

[113] Y. Choi, H. Kim, Y. Peng, A. Thomson, C. Lewandowski, R. Polski, Y. Zhang, H. S. Arora, K. Watanabe, T. Taniguchi, J. Alicea, and S. Nadj-Perge, Correlation-driven topological phases in magic-angle twisted bilayer graphene, Nature (London) **589**, 536 (2021).

[114] X. Liu, Z. Wang, K. Watanabe, T. Taniguchi, O. Vafek, and J. I. A. Li, Tuning electron correlation in magic-angle twisted

bilayer graphene using Coulomb screening, Science **371**, 1261 (2021).

[115] Y. Saito, J. Ge, L. Rademaker, K. Watanabe, T. Taniguchi, D. A. Abanin, and A. F. Young, Hofstadter subband ferromagnetism and symmetry-broken Chern insulators in twisted bilayer graphene, Nat. Phys. **17**, 478 (2021).

[116] Y. Xie, A. T. Pierce, J. M. Park, D. E. Parker, E. Khalaf, P. Ledwith, Y. Cao, S. H. Lee, S. Chen, P. R. Forrester, K. Watanabe, T. Taniguchi, A. Vishwanath, P. Jarillo-Herrero, and A. Yacoby, Fractional Chern insulators in magic-angle twisted bilayer graphene, Nature (London) **600**, 439 (2021).

[117] A. T. Pierce, Y. Xie, J. M. Park, E. Khalaf, S. H. Lee, Y. Cao, D. E. Parker, P. R. Forrester, S. Chen, K. Watanabe, T. Taniguchi, A. Vishwanath, P. Jarillo-Herrero, and A. Yacoby, Unconventional sequence of correlated Chern insulators in magic-angle twisted bilayer graphene, Nat. Phys. **17**, 1210 (2021).

[118] J. M. Park, Y. Cao, K. Watanabe, T. Taniguchi, and P. Jarillo-Herrero, Flavour Hund's coupling, Chern gaps and charge diffusivity in moiré graphene, Nature (London) **592**, 43 (2021).

[119] J.-X. Lin, Y.-H. Zhang, E. Morissette, Z. Wang, S. Liu, D. Rhodes, K. Watanabe, T. Taniguchi, J. Hone, and J. I. A. Li, Spin orbit driven ferromagnetism at half moiré filling in magic-angle twisted bilayer graphene, Science **375**, 437 (2022).

[120] S. Bhowmik, B. Ghawri, N. Leconte, S. Appalakondaiah, M. Pandey, P. S. Mahapatra, D. Lee, K. Watanabe, T. Taniguchi, J. Jung, A. Ghosh, and U. Chandni, Broken-symmetry states at half-integer band fillings in twisted bilayer graphene, Nat. Phys. **18**, 639 (2022).

[121] I. Das, C. Shen, A. Jaoui, J. Herzog-Arbeitman, A. Chew, C.-W. Cho, K. Watanabe, T. Taniguchi, B. A. Piot, B. A. Bernevig, and D. K. Efetov, Observation of reentrant correlated insulators and interaction-driven fermi-surface reconstructions at one magnetic flux quantum per moiré unit cell in magic-angle twisted bilayer graphene, Phys. Rev. Lett. **128**, 217701 (2022).

[122] R. Polski, Y. Zhang, Y. Peng, H. S. Arora, Y. Choi, H. Kim, K. Watanabe, T. Taniguchi, G. Refael, F. von Oppen, and S. Nadj-Perge, Hierarchy of symmetry breaking correlated phases in twisted bilayer graphene, arXiv:2205.05225.

[123] J. Yu, B. A. Foutty, Z. Han, M. E. Barber, Y. Schattner, K. Watanabe, T. Taniguchi, P. Phillips, Z.-X. Shen, S. A. Kivelson, and B. E. Feldman, Correlated Hofstadter spectrum and flavour phase diagram in magic-angle twisted bilayer graphene, Nat. Phys. **18**, 825 (2022).

[124] C.-C. Tseng, X. Ma, Z. Liu, K. Watanabe, T. Taniguchi, J.-H. Chu, and M. Yankowitz, Anomalous Hall effect at half filling in twisted bilayer graphene, Nat. Phys. **18**, 1038 (2022).

[125] S. Grover, M. Bocarsly, A. Uri, P. Stepanov, G. Di Battista, I. Roy, J. Xiao, A. Y. Meltzer, Y. Myasoedov, K. Pareek, K. Watanabe, T. Taniguchi, B. Yan, A. Stern, E. Berg, D. K. Efetov, and E. Zeldov, Chern mosaic and Berry-curvature magnetism in magic-angle graphene, Nat. Phys. **18**, 885 (2022).

[126] J. Díez-Mérida, A. Díez-Carlón, S. Y. Yang, Y.-M. Xie, X.-J. Gao, J. Senior, K. Watanabe, T. Taniguchi, X. Lu, A. P. Higginbotham, K. T. Law, and D. K. Efetov, Symmetry-broken Josephson junctions and superconducting diodes in

magic-angle twisted bilayer graphene, Nat. Commun. **14**, 2396 (2023).

[127] H. Tian, X. Gao, Y. Zhang, S. Che, T. Xu, P. Cheung, K. Watanabe, T. Taniguchi, M. Randeria, F. Zhang, C. N. Lau, and M. W. Bockrath, Evidence for Dirac flat band superconductivity enabled by quantum geometry, Nature (London) **614**, 440 (2023).

[128] A. Kerelsky, L. J. McGilly, D. M. Kennes, L. Xian, M. Yankowitz, S. Chen, K. Watanabe, T. Taniguchi, J. Hone, C. Dean, A. Rubio, and A. N. Pasupathy, Maximized electron interactions at the magic angle in twisted bilayer graphene, Nature (London) **572**, 95 (2019).

[129] Y. Jiang, X. Lai, K. Watanabe, T. Taniguchi, K. Haule, J. Mao, and E. Y. Andrei, Charge order and broken rotational symmetry in magic-angle twisted bilayer graphene, Nature (London) **573**, 91 (2019).

[130] S.-Y. Li, Y. Zhang, Y.-N. Ren, J. Liu, X. Dai, and L. He, Experimental evidence for orbital magnetic moments generated by moiré-scale current loops in twisted bilayer graphene, Phys. Rev. B **102**, 121406(R) (2020).

[131] Y. Choi, J. Kemmer, Y. Peng, A. Thomson, H. Arora, R. Polski, Y. Zhang, H. Ren, J. Alicea, G. Refael, F. von Oppen, K. Watanabe, T. Taniguchi, and S. Nadj-Perge, Electronic correlations in twisted bilayer graphene near the magic angle, Nat. Phys. **15**, 1174 (2019).

[132] X. Lu, B. Lian, G. Chaudhary, B. A. Piot, G. Romagnoli, K. Watanabe, T. Taniguchi, M. Poggio, A. H. MacDonald, B. A. Bernevig, and D. K. Efetov, Multiple flat bands and topological Hofstadter butterfly in twisted bilayer graphene close to the second magic angle, Proc. Natl. Acad. Sci. USA **118**, e2100006118 (2021).

[133] J. Finney, A. L. Sharpe, E. J. Fox, C. L. Hsueh, D. E. Parker, M. Yankowitz, S. Chen, K. Watanabe, T. Taniguchi, C. R. Dean, A. Vishwanath, M. A. Kastner, and D. Goldhaber-Gordon, Unusual magnetotransport in twisted bilayer graphene, Proc. Natl. Acad. Sci. USA **119**, e2118482119 (2022).

[134] Y. Zhang, R. Polski, C. Lewandowski, A. Thomson, Y. Peng, Y. Choi, H. Kim, K. Watanabe, T. Taniguchi, J. Alicea, F. von Oppen, G. Refael, and S. Nadj-Perge, Promotion of superconductivity in magic-angle graphene multilayers, Science **377**, 1538 (2022).

[135] X. Liu, N. J. Zhang, K. Watanabe, T. Taniguchi, and J. I. A. Li, Isospin order in superconducting magic-angle twisted trilayer graphene, Nat. Phys. **18**, 522 (2022).

[136] S. Hubmann, G. D. Battista, I. A. Dmitriev, K. Watanabe, T. Taniguchi, D. K. Efetov, and S. D. Ganichev, Infrared photoresistance as a sensitive probe of electronic transport in twisted bilayer graphene, 2D Mater. **10**, 015005 (2023).

[137] D. Guerci, P. Simon, and C. Mora, Moiré lattice effects on the orbital magnetic response of twisted bilayer graphene and condon instability, Phys. Rev. B **103**, 224436 (2021).

[138] Y. Avishai and Y. B. Band, Graphene bilayer and trilayer moiré lattice with Rashba spin-orbit coupling, Phys. Rev. B **106**, L041406 (2022).

[139] X. Lin and J. Ni, Effective lattice model of graphene moiré superlattices on hexagonal boron nitride, Phys. Rev. B **100**, 195413 (2019).

[140] X. Lin and J. Ni, Symmetry breaking in the double moiré superlattices of relaxed twisted bilayer graphene

on hexagonal boron nitride, Phys. Rev. B **102**, 035441 (2020).

[141] T. Cea, P. A. Pantaleón, and F. Guinea, Band structure of twisted bilayer graphene on hexagonal boron nitride, Phys. Rev. B **102**, 155136 (2020).

[142] X. Lin, K. Su, and J. Ni, Misalignment instability in magic-angle twisted bilayer graphene on hexagonal boron nitride, 2D Mater. **8**, 025025 (2021).

[143] J. Cao, F. Qi, H. Yang, and G. Jin, Superflat energy band induced by moiré electric potential in twisted bilayer graphene, Phys. Rev. B **103**, 165417 (2021).

[144] J. Shi, J. Zhu, and A. H. MacDonald, Moiré commensurability and the quantum anomalous Hall effect in twisted bilayer graphene on hexagonal boron nitride, Phys. Rev. B **103**, 075122 (2021).

[145] D. Mao and T. Senthil, Quasiperiodicity, band topology, and moiré graphene, Phys. Rev. B **103**, 115110 (2021).

[146] J. Shin, Y. Park, B. L. Chittari, J.-H. Sun, and J. Jung, Electron-hole asymmetry and band gaps of commensurate double moire patterns in twisted bilayer graphene on hexagonal boron nitride, Phys. Rev. B **103**, 075423 (2021).

[147] M. Long, P. A. Pantaleón, Z. Zhan, F. Guinea, J. Á. Silva-Guillén, and S. Yuan, An atomistic approach for the structural and electronic properties of twisted bilayer graphene-boron nitride heterostructures, npj Comput. Mater. **8**, 73 (2022).

[148] Y. Chen, W.-T. Guo, Z.-S. Chen, S. Wang, and J.-M. Zhang, First-principles study on the heterostructure of twisted graphene/hexagonal boron nitride/graphene sandwich structure, J. Phys.: Condens. Matter **34**, 125504 (2022).

[149] M. Long, Z. Zhan, P. A. Pantaleón, J. A. Silva-Guillén, F. Guinea, and S. Yuan, Electronic properties of twisted bilayer graphene suspended and encapsulated with hexagonal boron nitride, Phys. Rev. B **107**, 115140 (2023).

[150] X. Lin, Q. Zhou, C. Li, and J. Ni, Collective excitations of the Chern-insulator states in commensurate double moiré superlattices of twisted bilayer graphene on hexagonal boron nitride, Phys. Rev. B **107**, 195434 (2023).

[151] G. Wagner, Y. H. Kwan, N. Bultinck, S. H. Simon, and S. A. Parameswaran, Global phase diagram of the normal state of twisted bilayer graphene, Phys. Rev. Lett. **128**, 156401 (2022).

[152] H. C. Po, L. Zou, T. Senthil, and A. Vishwanath, Faithful tight-binding models and fragile topology of magic-angle bilayer graphene, Phys. Rev. B **99**, 195455 (2019).

[153] H. Shi and X. Dai, Heavy-fermion representation for twisted bilayer graphene systems, Phys. Rev. B **106**, 245129 (2022).

[154] K. Singh, A. Chew, J. Herzog-Arbeitman, B. A. Bernevig, and O. Vafek, Topological heavy fermions in magnetic field, arXiv:2305.08171.

[155] Y. Hasegawa and M. Kohmoto, Periodic Landau gauge and quantum Hall effect in twisted bilayer graphene, Phys. Rev. B **88**, 125426 (2013).

[156] M. Fujimoto and M. Koshino, Moiré edge states in twisted bilayer graphene and their topological relation to quantum pumping, Phys. Rev. B **103**, 155410 (2021).

[157] E. Andrade, P. A. Pantaleón, F. Guinea, and G. G. Naumis, Flat bands and electronic localization in twisted bilayer graphene nanoribbons, Phys. Rev. B **108**, 235418 (2023).

[158] P. Streda, Theory of quantised Hall conductivity in two dimensions, J. Phys. C **15**, L717 (1982).

[159] R. Bistritzer and A. H. MacDonald, Moiré butterflies in twisted bilayer graphene, Phys. Rev. B **84**, 035440 (2011).

[160] M.-Y. Choi, Y.-H. Hyun, and Y. Kim, Angle dependence of the Landau level spectrum in twisted bilayer graphene, Phys. Rev. B **84**, 195437 (2011).

[161] Y.-H. Zhang, H. C. Po, and T. Senthil, Landau level degeneracy in twisted bilayer graphene: Role of symmetry breaking, Phys. Rev. B **100**, 125104 (2019).

[162] K. Hejazi, C. Liu, and L. Balents, Landau levels in twisted bilayer graphene and semiclassical orbits, Phys. Rev. B **100**, 035115 (2019).

[163] B. Lian, F. Xie, and B. A. Bernevig, Landau level of fragile topology, Phys. Rev. B **102**, 041402(R) (2020).

[164] J. Herzog-Arbeitman, Z.-D. Song, N. Regnault, and B. A. Bernevig, Hofstadter topology: Noncrystalline topological materials at high flux, Phys. Rev. Lett. **125**, 236804 (2020).

[165] B. Andrews and A. Soluyanov, Fractional quantum Hall states for moiré superstructures in the Hofstadter regime, Phys. Rev. B **101**, 235312 (2020).

[166] Y. Sheffer and A. Stern, Chiral magic-angle twisted bilayer graphene in a magnetic field: Landau level correspondence, exact wave functions, and fractional Chern insulators, Phys. Rev. B **104**, L121405 (2021).

[167] B. Lian, F. Xie, and B. A. Bernevig, Open momentum space method for the Hofstadter butterfly and the quantized Lorentz susceptibility, Phys. Rev. B **103**, L161405 (2021).

[168] J. Kang, B. A. Bernevig, and O. Vafek, Cascades between light and heavy fermions in the normal state of magic-angle twisted bilayer graphene, Phys. Rev. Lett. **127**, 266402 (2021).

[169] Y. Hwang, J.-W. Rhim, and B.-J. Yang, Geometric characterization of anomalous Landau levels of isolated flat bands, Nat. Commun. **12**, 6433 (2021).

[170] N. Benlakhouy, A. Jellal, H. Bahlouli, and M. Vogl, Chiral limits and effect of light on the Hofstadter butterfly in twisted bilayer graphene, Phys. Rev. B **105**, 125423 (2022).

[171] Y. Guan, A. Bouhon, and O. V. Yazyev, Landau levels of the Euler class topology, Phys. Rev. Res. **4**, 023188 (2022).

[172] T.-N. Do, P.-H. Shih, H. Lin, D. Huang, G. Gumbs, and T.-R. Chang, Generalized Peierls substitution for the tight-binding model of twisted graphene systems in a magnetic field, Phys. Rev. B **105**, 235418 (2022).

[173] J. Herzog-Arbeitman, A. Chew, and B. A. Bernevig, Magnetic Bloch theorem and reentrant flat bands in twisted bilayer graphene at 2π flux, Phys. Rev. B **106**, 085140 (2022).

[174] J. Herzog-Arbeitman, A. Chew, D. K. Efetov, and B. A. Bernevig, Reentrant correlated insulators in twisted bilayer graphene at 25 t (2π flux), Phys. Rev. Lett. **129**, 076401 (2022).

[175] N. Paul, P. J. D. Crowley, T. Devakul, and L. Fu, Moiré Landau fans and magic zeros, Phys. Rev. Lett. **129**, 116804 (2022).

[176] X. Wang and O. Vafek, Narrow bands in magnetic field and strong-coupling Hofstadter spectra, Phys. Rev. B **106**, L121111 (2022).

[177] L. A. Navarro-Labastida and G. G. Naumis, 3/2 magic angle quantization rule of flat bands in twisted bilayer graphene and its relationship to the quantum Hall effect, Phys. Rev. B **107**, 155428 (2023).

[178] J. Herzog-Arbeitman, Z.-D. Song, L. Elcoro, and B. A. Bernevig, Hofstadter topology with real space invariants and

reentrant projective symmetries, Phys. Rev. Lett. **130**, 236601 (2023).

[179] D. Shaffer, J. Wang, and L. H. Santos, Unconventional self-similar Hofstadter superconductivity from repulsive interactions, Nat. Commun. **13**, 7785 (2022).

[180] P. Moon and M. Koshino, Energy spectrum and quantum Hall effect in twisted bilayer graphene, Phys. Rev. B **85**, 195458 (2012).

[181] Y. Guan, O. V. Yazyev, and A. Kruchkov, Reentrant magic-angle phenomena in twisted bilayer graphene in integer magnetic fluxes, Phys. Rev. B **106**, L121115 (2022).

[182] Z. F. Wang, F. Liu, and M. Y. Chou, Fractal Landau-level spectra in twisted bilayer graphene, Nano Lett. **12**, 3833 (2012).

[183] P. Moon and M. Koshino, Optical properties of the Hofstadter butterfly in the moiré superlattice, Phys. Rev. B **88**, 241412(R) (2013).

[184] K. Uchida, S. Furuya, J.-I. Iwata, and A. Oshiyama, Atomic corrugation and electron localization due to moiré patterns in twisted bilayer graphenes, Phys. Rev. B **90**, 155451 (2014).

[185] E. Polizzi, Density-matrix-based algorithm for solving eigenvalue problems, Phys. Rev. B **79**, 115112 (2009).

[186] G. Trambly de Laissardière, D. Mayou, and L. Magaud, Localization of Dirac electrons in rotated graphene bilayers, Nano Lett. **10**, 804 (2010).

[187] P. Lucignano, D. Alfè, V. Cataudella, D. Ninno, and G. Cantele, Crucial role of atomic corrugation on the flat bands and energy gaps of twisted bilayer graphene at the magic angle $\theta \sim 1.08°$, Phys. Rev. B **99**, 195419 (2019).

[188] K. Zollner, M. Gmitra, and J. Fabian, Heterostructures of graphene and hBN: Electronic, spin-orbit, and spin relaxation properties from first principles, Phys. Rev. B **99**, 125151 (2019).

[189] K. Zollner, A. W. Cummings, S. Roche, and J. Fabian, Graphene on two-dimensional hexagonal BN, AlN, and GaN: Electronic, spin-orbit, and spin relaxation properties, Phys. Rev. B **103**, 075129 (2021).

[190] G. H. Wannier, A result not dependent on rationality for Bloch electrons in a magnetic field, Physica Status Solidi B **88**, 757 (1978).

[191] S. Carr, S. Fang, P. Jarillo-Herrero, and E. Kaxiras, Pressure dependence of the magic twist angle in graphene superlattices, Phys. Rev. B **98**, 085144 (2018).

[192] S. Carr, S. Fang, and E. Kaxiras, Electronic-structure methods for twisted moiré layers, Nat. Rev. Mater. **5**, 748 (2020).

[193] S. Fang, S. Carr, Z. Zhu, D. Massatt, and E. Kaxiras, Angle-dependent *ab initio* low-energy Hamiltonians for a relaxed twisted bilayer graphene heterostructure, arXiv:1908.00058.

[194] L.-J. Yin, L.-H. Tong, Y.-Y. Zhou, Y. Zhang, Y. Tian, L. Zhang, L. Zhang, and Z. Qin, Direct observation of moiré flat-band breakdown at the edge of magic-angle twisted bilayer graphene, Phys. Rev. B **105**, L201405 (2022).

[195] A. Khalifa, G. Murthy, and R. K. Kaul, Absence of edge states in the valley Chern insulator in moiré graphene, Phys. Rev. B **107**, 085138 (2023).

[196] P. Törmä, S. Peotta, and B. A. Bernevig, Superconductivity, superfluidity and quantum geometry in twisted multilayer systems, Nat. Rev. Phys. **4**, 528 (2022).

[197] K. P. Nuckolls, R. L. Lee, M. Oh, D. Wong, T. Soejima, J. P. Hong, D. Călugăru, J. Herzog Arbeitman, B. A. Bernevig, K. Watanabe, T. Taniguchi, N. Regnault, M. P. Zaletel, and A. Yazdani, Quantum textures of the many-body wavefunctions in magic-angle graphene, Nature (London) **620**, 525 (2023).

[198] M. Fortin-Deschenes, R. Pu, Y.-F. Zhou, C. Ma, P. Cheung, K. Watanabe, T. Taniguchi, F. Zhang, X. Du, and F. Xia, Uncovering topological edge states in twisted bilayer graphene, Nano Lett. **22**, 6186 (2022).

[199] J. Sichau, M. Prada, T. Anlauf, T. J. Lyon, B. Bosnjak, L. Tiemann, and R. H. Blick, Resonance microwave measurements of an intrinsic spin-orbit coupling gap in graphene: A possible indication of a topological state, Phys. Rev. Lett. **122**, 046403 (2019).

[200] U. R. Singh, M. Prada, V. Strenzke, B. Bosnjak, T. Schmirander, L. Tiemann, and R. H. Blick, Sublattice symmetry breaking and ultralow energy excitations in graphene-on-*h*BN heterostructures, Phys. Rev. B **102**, 245134 (2020).

[201] L. Tiemann, M. Prada, V. Strenzke, and R. H. Blick, Comment on "Electron spin resonance and collective excitations in magic-angle twisted bilayer graphene," arXiv:2206.14628.

[202] M. Fleischmann, R. Gupta, D. Weckbecker, W. Landgraf, O. Pankratov, V. Meded, and S. Shallcross, Moiré edge states in twisted graphene nanoribbons, Phys. Rev. B **97**, 205128 (2018).

[203] G. Trambly de Laissardière, D. Mayou, and L. Magaud, Numerical studies of confined states in rotated bilayers of graphene, Phys. Rev. B **86**, 125413 (2012).

[204] A. O. Sboychakov, A. L. Rakhmanov, A. V. Rozhkov, and F. Nori, Electronic spectrum of twisted bilayer graphene, Phys. Rev. B **92**, 075402 (2015).

[205] S. Fang and E. Kaxiras, Electronic structure theory of weakly interacting bilayers, Phys. Rev. B **93**, 235153 (2016).

[206] L. Rademaker, D. A. Abanin, and P. Mellado, Charge smoothening and band flattening due to Hartree corrections in twisted bilayer graphene, Phys. Rev. B **100**, 205114 (2019).

[207] T. Löthman, J. Schmidt, F. Parhizgar, and A. M. Black-Schaffer, Nematic superconductivity in magic-angle twisted bilayer graphene from atomistic modeling, Commun. Phys. **5**, 92 (2022).

[208] J. Kang and O. Vafek, Pseudomagnetic fields, particle-hole asymmetry, and microscopic effective continuum Hamiltonians of twisted bilayer graphene, Phys. Rev. B **107**, 075408 (2023).

[209] O. Vafek and J. Kang, Continuum effective Hamiltonian for graphene bilayers for an arbitrary smooth lattice deformation from microscopic theories, Phys. Rev. B **107**, 075123 (2023).

[210] W. Miao, C. Li, X. Han, D. Pan, and X. Dai, Truncated atomic plane wave method for subband structure calculations of moiré systems, Phys. Rev. B **107**, 125112 (2023).

[211] https://www.alliancecan.ca/.